Computer Simulation of High Current Uranium Beams for the Injection Beam Line of the UNILAC

W. Xiang

Institute of Electronic Engineering, China Academy of Engineering Physics
P.O. Box 919-523, Mianyang 621900, Sichuan, China
P. Spädtke, R. Hollinger, M. Galonska, F. Heymach
Gesellschaft für Schwerionenforschung mbH, Planckstr. 1, 64291 Darmstadt, Germany

1 Introduction

The MEVVA ion source has been developed to provide high current beams of multiply charged metal ions over the last two decades primarily for material modification [1,2]. It has been investigated since then at GSI for accelerator application [3,4]. To achieve a high particle current to fill up the heavy ion synchrotron SIS to its space charge limit, many efforts have been made at GSI, to increase the beam brightness, to enhance the fraction of charge state 4^+ for the design ion ^{238}U [5-7], to reduce the beam noise [8-10], and to improve the beam stability [11]. For the extraction of the desired uranium ion beam, a multi-aperture triode extraction system with optimum aspect ratio is used due to high mass-to-charge ratio of the design ion [12]. In general, the three-electrode extraction system is limited in beam energy to several tens of kilovolts due to power loading on the electrodes and high voltage holding ability [13]. Therefore, a post-acceleration system is required at GSI to achieve the specific input energy of the RFQ of 2.2 keV/u; i.e. the total voltage drop for U^{4+} ion of 130.9 kV is separated into an extraction voltage and an acceleration voltage. The advantage of separation is the possibility to match the extraction field strength to the source plasma condition independently from the desired ion energy; however, the combination of the extraction system and the post-acceleration system has a strong influence on the beam quality [11,14]. Advances in vacuum arc ion source development to the benefit of uranium beam time at the GSI facility can be found in [15], results of recent vacuum arc ion source (VARIS) development is reported in [16].

In an attempt to generate an ion beam with high current and high brightness for the design ion, the computer code KOBRA3-INP [17] has been used to evaluate the extraction system, the DC post-acceleration system as well as the quadrupole transport beam line, and to study the behavior of the ion beam in the combined system.

2 Simulation method

All simulations were made using the programs KOBRA3-INP and MAG2KOB3-INP [17]. These interactive programs run on a PC with reasonable computing time for the solver for the given problem with reasonable accuracy.

KOBRA3-INP translates the geometry information into mesh information and solves first the Laplace equation on a fully 3D Cartesian mesh, using the finite difference method (FDM). For the solution of the set of equations an iterative point-to-point successive over-relaxation (SOR) method is used. Ray tracing is made by exact integration. Eventually existing magnetic fields are used for the ray tracing. They have to be provided on the same mesh as it is used for the geometry and for the potential. By repeated solving of Poisson equation, ray tracing, and re-determination of the space charge distribution a self-consistent solution can be found. An important feature of this code is that existing boundaries between regions with space charge and regions with plasma conditions are taken into account.

The program gives the choice of a static ray tracing for a time-dependent particle in cell (PIC) solution. Because the investigated problem is steady state, the ray tracing method has been used here. Crucial points of the simulation are the partially unknown starting conditions of the ions, as well as an analytic description of the existing space charge compensation.

The program has been used successfully up to now to simulate the extraction for electron guns and ion sources of the duoplasmatron type, multicusp ion sources, surface ionization ion sources, Penning ion sources, laser ion sources, electron cyclotron resonance ion sources, and metal vacuum arc ion sources, as well as H⁻ sources [18]. For each plasma generator the starting conditions of the particles and all other parameters have to be adapted.

The simulation covers the ion beam extraction, acceleration, matching with magnetic quadrupoles to the spectrometer, and the connecting drift sections. The strategy of simulation is described in section 4.

3 Experimental setup

Fig.2 shows a layout of part of the low energy beam line for delivering the ion beam extracted from the MEVVA source to the RFQ injector. This beam line is installed at the high current injector (HSI [19,14,20]) at GSI. Tab.1 presents the technical operating conditions for the MEVVA ion source.

Tab.1 Technical operating conditions for the MEVVA and VARIS ion sources [15,16]

Arc voltage / current	50 V / 600-700 A, pulsed: 1 Hz, 1ms
Flux density solenoid I / II	40 mT / 0-60 mT (VARIS)
Cathode diameter	5.7 mm
Distance between cathode and anode	15 mm (VARIS)
Anode aperture	15 mm
Anode material	Stainless steel
Extraction apertures	13×3 mm
Aspect ratio	0.5
Extraction voltage	32 kV
Screening voltage	-1.5 kV

To generate a high current ion beam at low energy, a well-optimized multi-aperture accel-decel extraction system with 13 holes, each 3 mm in diameter is used. The detailed geometry of the extraction system and potentials applied are shown in Fig.1. The distances between the electrodes are 3 mm and 1 mm; the applied voltages are 32 kV and -1.5 kV, respectively.
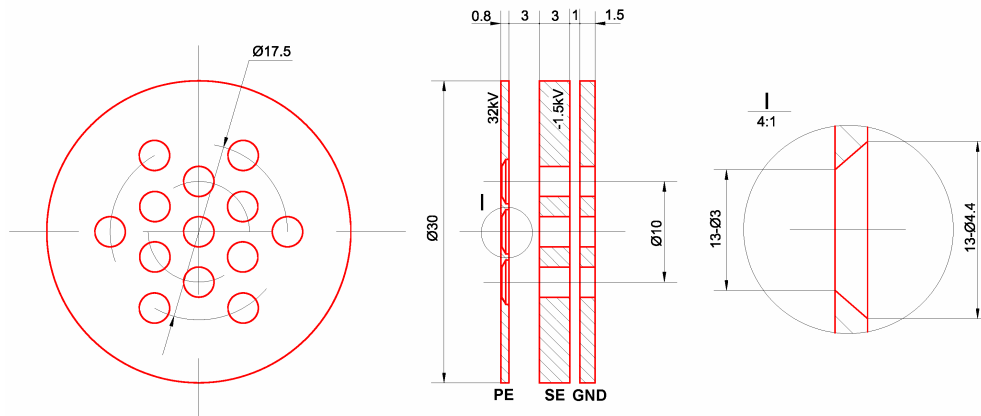

Fig.1 Detailed geometry of the extraction system and potentials applied to the electrodes. PE, plasma electrode; SE, screening electrode; GND, ground electrode.

A moveable, single acceleration gap is located about 900 mm behind the extraction system. In Fig.3, schematic of the post-acceleration system and potentials applied are shown. The acceleration system consists of a high voltage electrode, a ground electrode, a screening electrode and a second ground electrode. The acceleration voltage and screening voltage are 98.9 kV and -4.3 kV for uranium mode, respectively.

All data have been measured during regular uranium beam times in 2003. Typical measured ion beam currents and charge state distribution for the MEVVA ion source are listed in Tab.3.
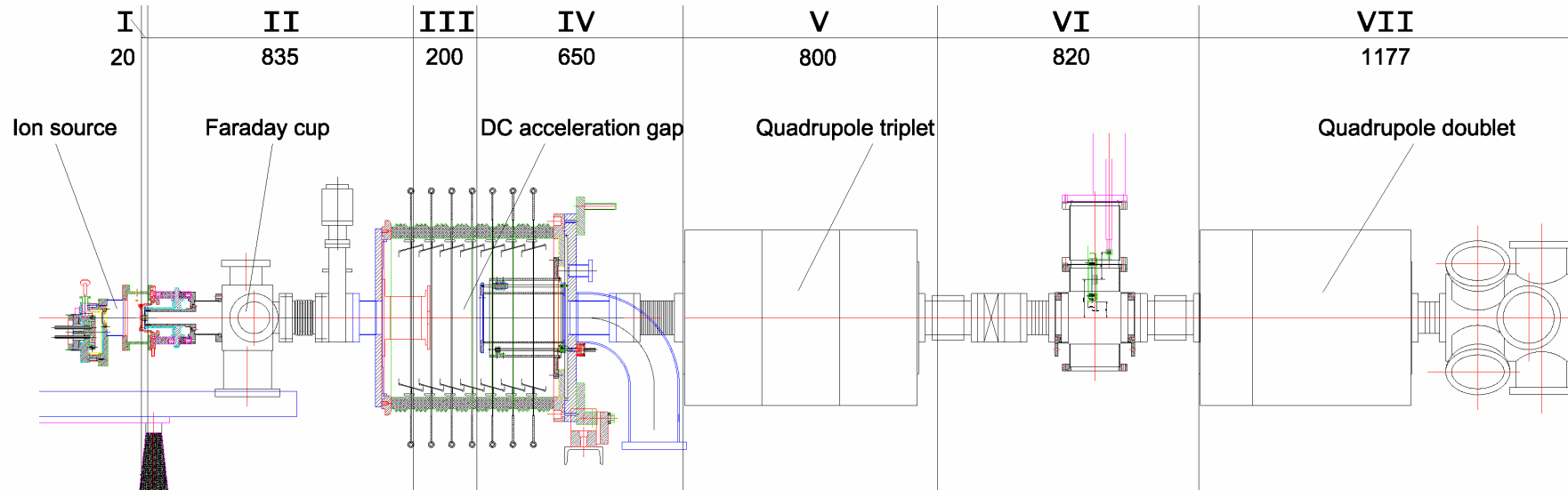
Fig.2 Layout of part of the low energy beam line. Simulation of the beam line is divided into seven sections. I, extraction; II, first drift; III, DC post-acceleration; IV, second drift; V, quadrupole triplet; VI, third drift; VII, quadrupole doublet.

Tab.2 Necessary computer CPU time for different sections

| Sections		Number of nodes	Number of trajectories	Iterations	Computer CPU time[*] (s)			
					Laplace	Poisson	Ray tracing	Total
I	Extraction	4.583.001	15.600	5	2.113	27.036	725	29.874
II	First drift	625.128	3.653	1			47	47
III	Acceleration	747.921	2.661	5	280	1.737	70	2.087
IV	Second drift	487.451	1.257	1			13	13
V	Quadrupole triplet	747.921	1.257	1			19	19
VI	Third drift	766.526	1.241	1			19	19
VII	Quadrupole doublet	1.160.952	1.199	1			24	24
Total								32.083

[*] Pentium IV, CPU 3.0 GHz, 1GB RAM
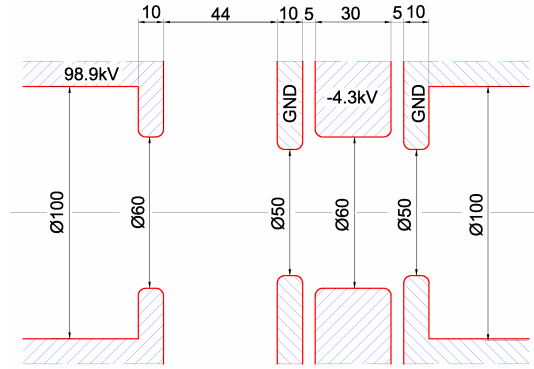
Fig.3 Schematic of DC post-acceleration system and potentials applied to the electrodes. From left to right: high voltage electrode, GND, SE, and GND electrode.

Tab.3 Measured ion beam currents and charge state distribution [6,16,21,22]

Ion charge state (current fraction)	(20% U^{3+}, 68% U^{4+} and 12% U^{5+})*
Longitudinal ion energy	188 eV (40-200 eV)*
Transverse ion energy	100 eV (0-150 eV)*
Electron temperature	11 eV (0-20 eV)*
Plasma potential hump	10 V (0-100 V)*
Emission current density	170 mA/cm^2 (110-270 mA/cm^2)*
Full beam ion beam current	156 mA@35 kV (135-140mA@32 kV)#
DC accelerated ion beam current	55 mA@131 kV (45-50mA@32 kV+98.9 kV)#

* Input parameters of uranium plasma for simulation
# Regular working parameters

4 Theoretical assumptions

4.0 Simulation

Simulation of the beam line is divided into seven sections, see Fig.2. They are extraction, first drift, DC post-acceleration, second drift, quadrupole triplet, third drift and quadrupole doublet, respectively. Numbers of nodes and trajectories, iterations, and computer CPU time of different sections are listed in Tab.2. The computer CPU time increases with the number of nodes and with the number of main iterations. Most of the time is used for the solution of Poisson's equation, especially if strong nonlinear fields are present as for example at the location of the plasma boundary. Therefore it is recommended to use the potential solution for one set of parameters as a starting solution for a modified set of parameters. Instead of the usually used five iterations only two main iterations are required for example for the scan of current density in the extraction system for each current density. For such a scan with six different values, fifteen (5+5×2) instead of thirty (6×5) iterations already halves the necessary computer CPU time. A further decrease can be achieved by controlling the number of iterations for the successive over relaxation method. This number can be reduced if the potential change becomes small between main iterations.

Inside the plasma a homogeneous ion density distribution is assumed. The starting energy is given by a directed ion drift energy which is determined by the physics of plasma formation and the ion temperature. Corresponding data for MEVVA ion sources have been measured [16,22]. The output coordinates of all particles at the end of the previous section are regarded as starting conditions for the next section. Compared to the section of extraction the other six sections are much less time consumptive. The section with the acceleration gap requires three iterations to become convergent. In all other sections only ray tracing is required because full space charge compensation is assumed.

4.1 Ion beam extraction

A plasma potential hump of 10 V is assumed in the simulation in this section according to the experimental measurement [22]. In addition, the space charge inside the plasma is compensated by electrons assumed to have a Boltzman density distribution [23]. In fact, the one of the distinct advantages of the accel-decel configuration is to suppress electrons back streaming to the ion source, and so here the accel-decel system is used to preserve the space charge compensation of the extracted ion beam. The space charge compensation behind the screening electrode is performed in the simulation only if the negative potential for all trajectories is sufficient to prevent electrons from back streaming to the source. For the simulation a potential of -10 V on axis is assumed to build up a potential hump for electrons generated in the beam channel. Fig.4 shows a typical space charge map and corresponding plasma boundary for the extraction system. Note, the space charge does not exist behind the screening electrode, i.e. the extracted ion beam is totally space charge neutralized.
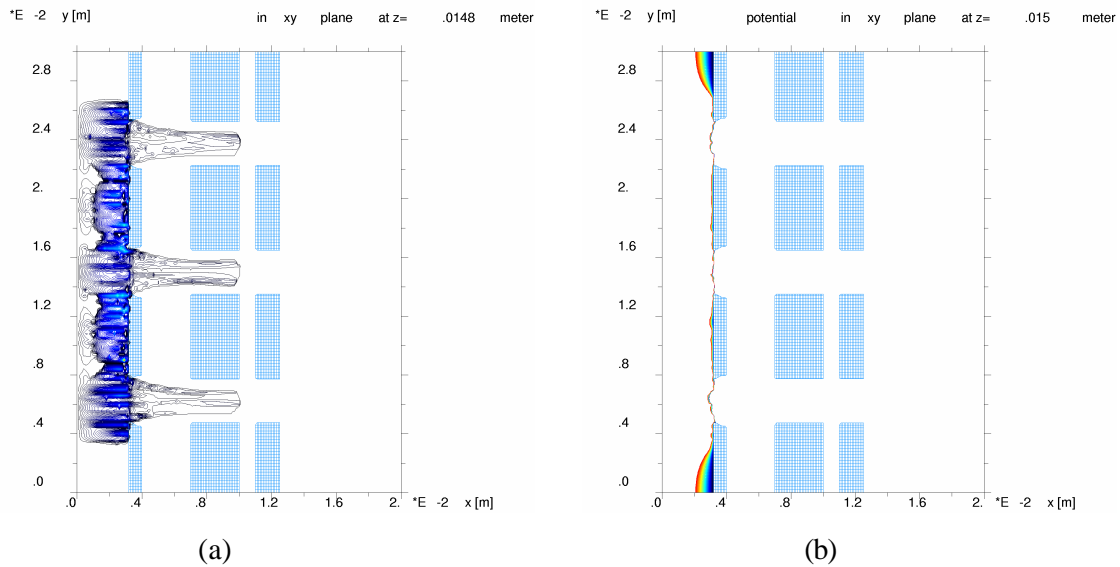

(a)   (b)

Fig.4 Typical space charge map (a) and corresponding plasma boundary (b) for the extraction system. From left to right: PE, SE, and GND electrode.

4.2 First drift

In general, more than 100 mA total uranium ion beam at 32 kV has to be extracted with above mentioned multi-aperture extraction system from the MEVVA ion source to meet the requirement of the synchrotron at GSI. Moreover, strong beam losses occur within all sections, therefore the influence of the space charge or possibly existing space charge compensation has to be taken into account in this section. The uranium ion beam propagates in this drift space at ground potential on the platform, and from experimental experience we strongly believe that its space charge is neutralized by the presence of electrons. The electrons may be generated by either the ionization of residual gases or sputtering [18]. Fig.5 and Fig.6 show the results for two models of the space charge compensation which can be used in the simulation. The degree of the space charge compensation has been varied from 0% to 100%. The first model assumes a linear compensation. The real current is replaced by an effective current. The corresponding results are shown in Fig.5. The second model assumes the presence of electrons with a certain energy distribution. Self's model [23] is applied to calculate the effective space charge potential The resulting trajectory plots and corresponding emittance plots in Fig. 6 demonstrate the influence of the degree of the space charge compensation. The applied model for the space charge compensation is responsible whether the beam transport will suffer from emittance growth. Using the beam plasma model, the potential becomes constant within the beam. At the beam edge the potential drops, causing a diverging force which is the reason for producing a beam halo, and simultaneously an emittance growth. For both cases, it can be concluded that the

transport of a beam with such intensities and such low energies would not be possible without a very high degree of the space charge compensation.

In all following simulations, 100% space charge compensation is assumed throughout the drift section from the ion source to the acceleration gap as well as for the beam transport sections behind the acceleration gap.
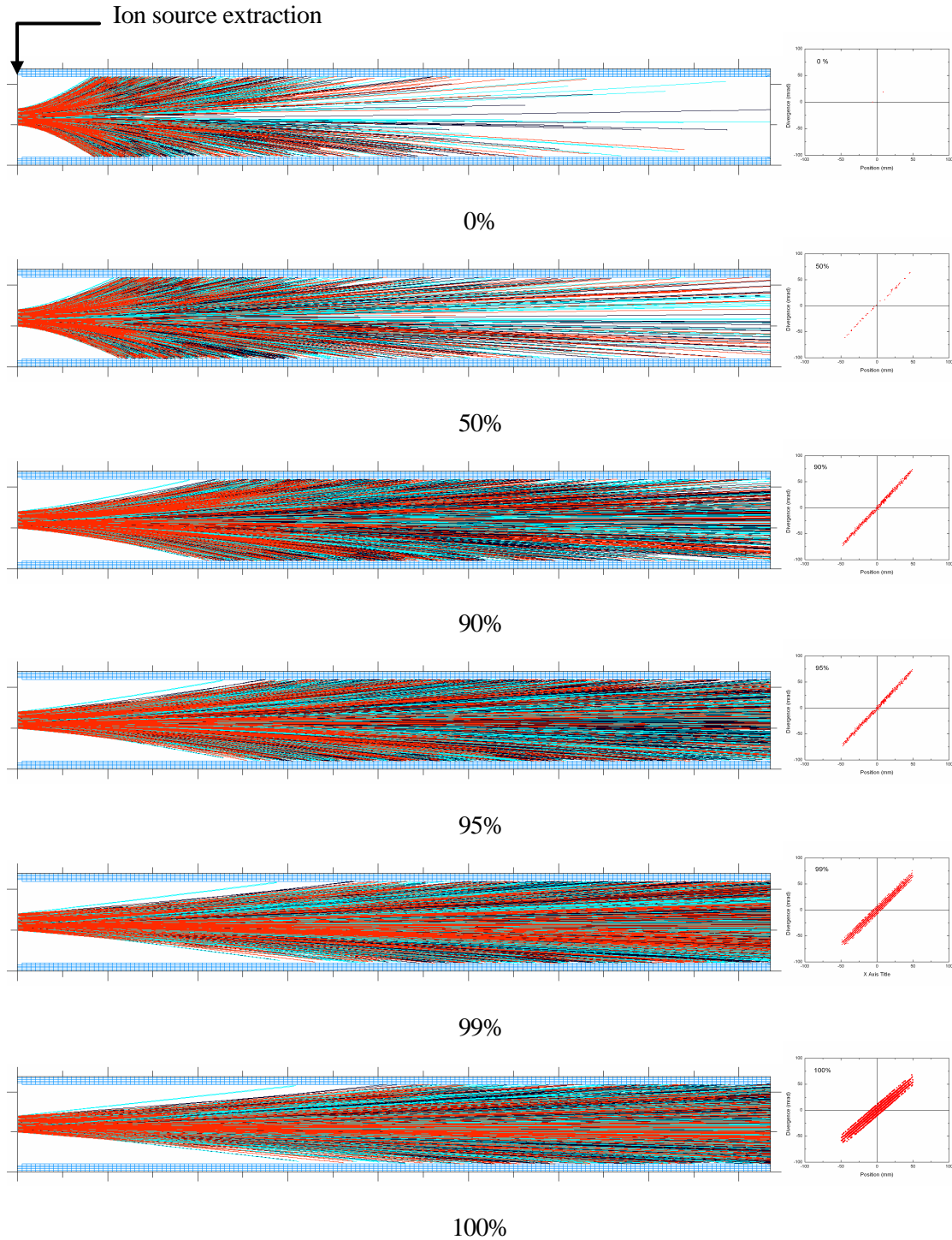
Ion source extraction

0%

50%

90%

95%

99%

100%

Fig.5 Trajectory plots and corresponding emittance diagrams for different degrees of the linear space charge compensation

7

Ion source extraction

0%

50%

90%

95%

99%

100%
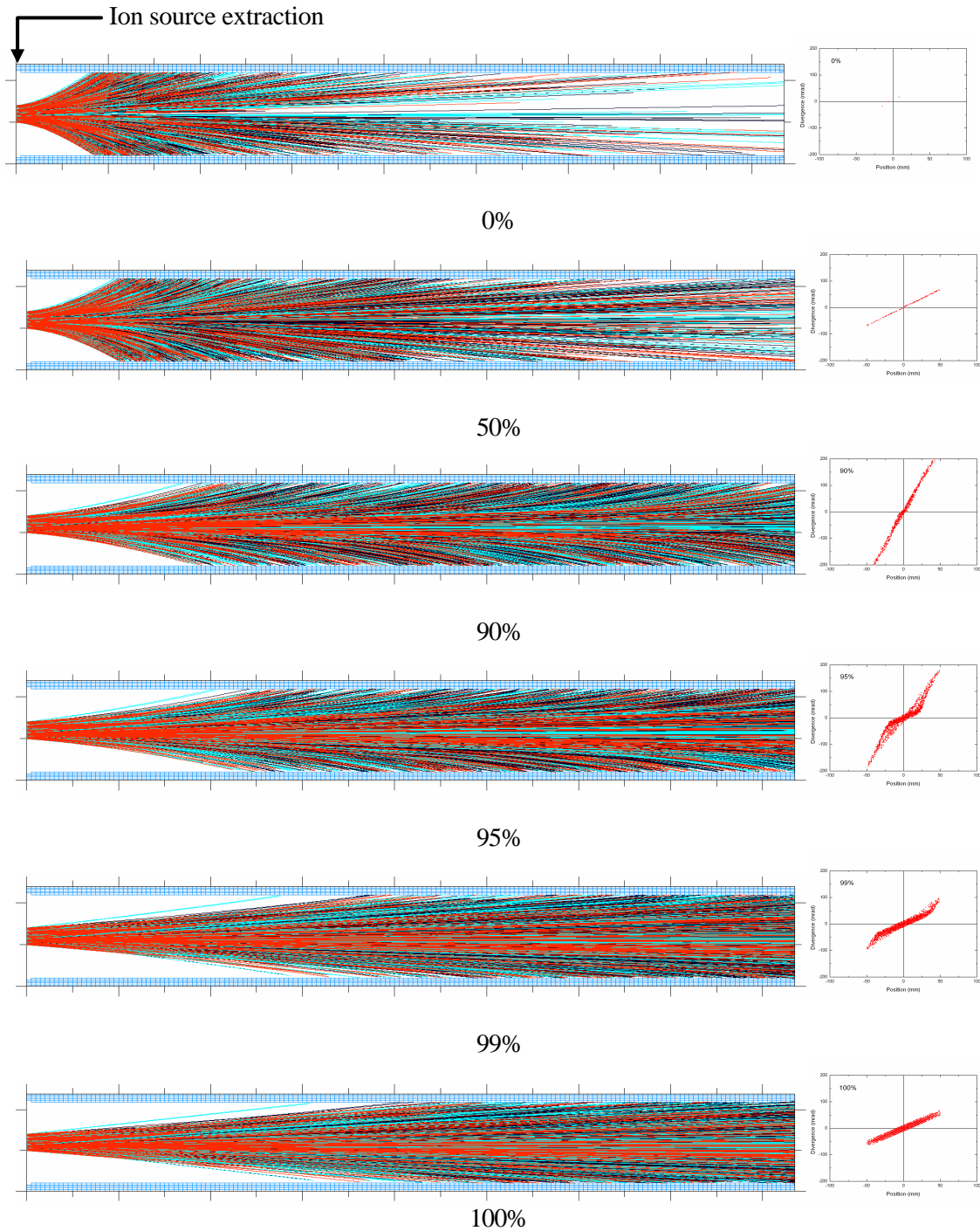
Fig.6 Trajectory plots and corresponding emittance diagrams for different degrees of the space charge compensation in terms of Self's model

4.3 DC post-acceleration

The function of the negative screening electrode behind the acceleration gap is to preserve the space charge compensation of the beam on ground potential [24]. On the high voltage platform the beam is assumed to be space charge compensated whereas in the acceleration gap no space charge compensation is present. A beam plasma boundary, similar to the extraction, will form. Another boundary will develop behind the screening electrode. The typical space charge map and corresponding plasma boundary for this section are shown in Fig.7.

8

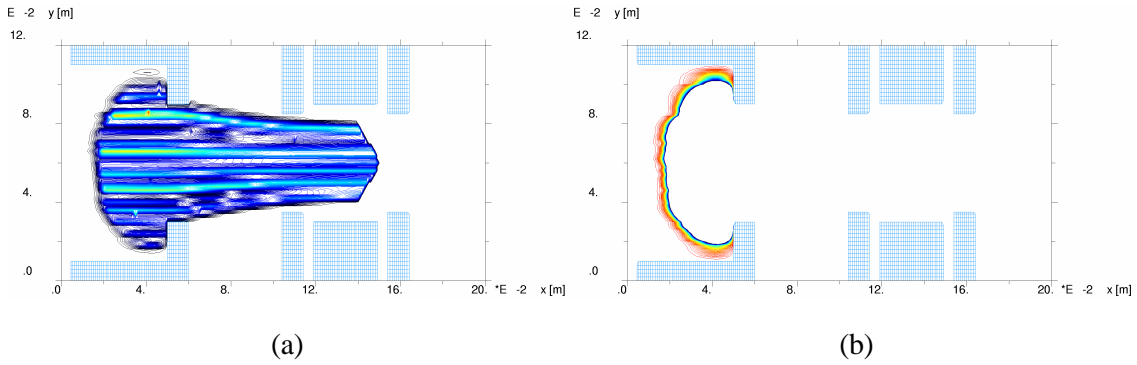(a)   (b)

Fig.7 Typical space charge map (a) and corresponding plasma boundary (b) for the acceleration gap. From left to right: HV, GND, SE and GND electrode.

4.4 Second drift

In this section, also 100% space charge compensation is assumed behind the screening electrode of the acceleration gap.

4.5 Quadrupole triplet

The magnetic field for this section has been created by the program MAG2KOB3-INP [17], using the field measurements given in the technical report [25]. Saturation effects and fringing field were taken into account. The actual setting of all quadrupoles from the beam time with uranium ions has been used. Lines of constant |B| are shown in Fig.8. The gradients and corresponding integration of the magnetic flux density of the quadrupole triplet along the beam line are shown in Fig.9.
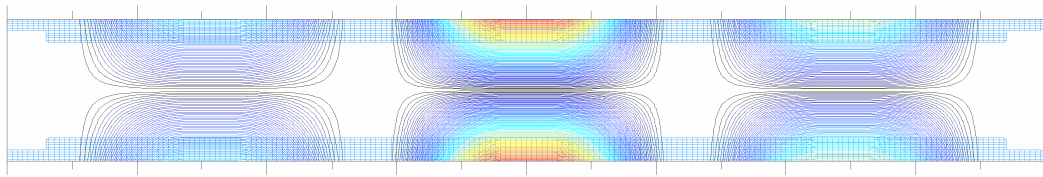

Fig.8 Magnetic flux density map in the mid-plane of the quadrupole triplet (Quadrupole settings [int. gradients]: -0.6149/1.3534/-0.8914 [T])
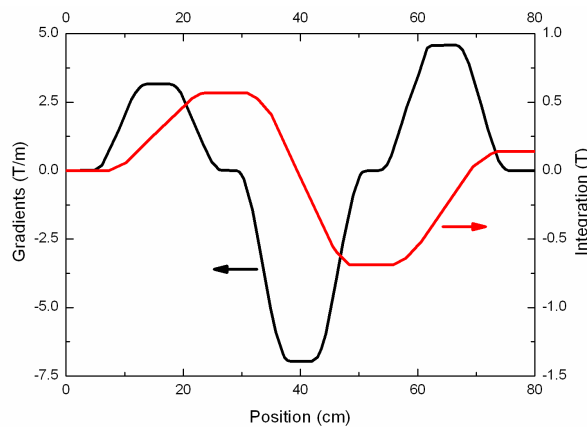

Fig.9 The gradients and corresponding integration of magnetic flux density of the quadrupole triplet along the beam line

4.6 Third drift

Also 100% space charge compensation is assumed in this section.

4.7 Quadrupole doublet

The magnetic flux density in the mid-plane of the quadrupole doublet is shown in Fig.10 [26]. The gradients and corresponding integration of the magnetic flux density of the quadrupole doublet along the beam line are shown in Fig.11.
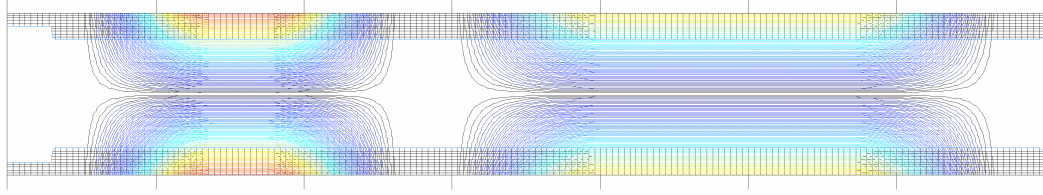

Fig.10 Magnetic flux density map in the mid-plane of the quadrupole doublet (Quadrupole settings [int. gradients]: 1.0018/-1.6639 [T])
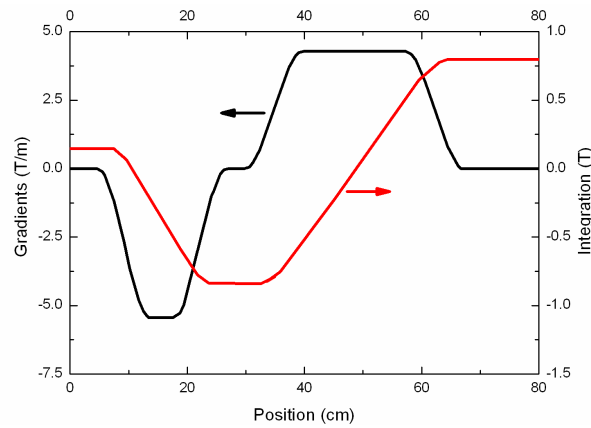

Fig.11 The gradients and corresponding integration of magnetic flux density of the quadrupole doublet along the beam line

5. Results and discussions

In the simulation all available information from the experiment has been used. By varying unknown parameters it was tried to reproduce the experimental beam properties by the simulation.

5.1 Effect of plasma parameters in MEVVA ion sources

5.1.1 Electron temperature

Fig.12 shows the dependence of the intensity and emittance of the ion beam on the electron temperature with a longitudinal ion energy of 160 eV, a transverse ion energy of 100 eV, a plasma potential hump of 10 V, and an emission current density of 180 mA/cm². One can note that the extracted ion beam current is not sensitive to the electron temperature. At the electron temperature lower than 10 eV, with increasing the electron temperature the intensity of the ion beam except for that of the extracted ion beam decreases and the emittance of the extracted ion beam increases. But when the electron temperature is up to 10 eV, the electron temperature has a slight influence on the intensity and emittance of the ion beam. Moreover, that the absolute emittance of the extracted and accelerated ion beam does not scale with $(32/(32+98.9))^{0.5}$ indicates the strong influence of the space charge. In the following simulation the electron temperature is specified to 5 eV.
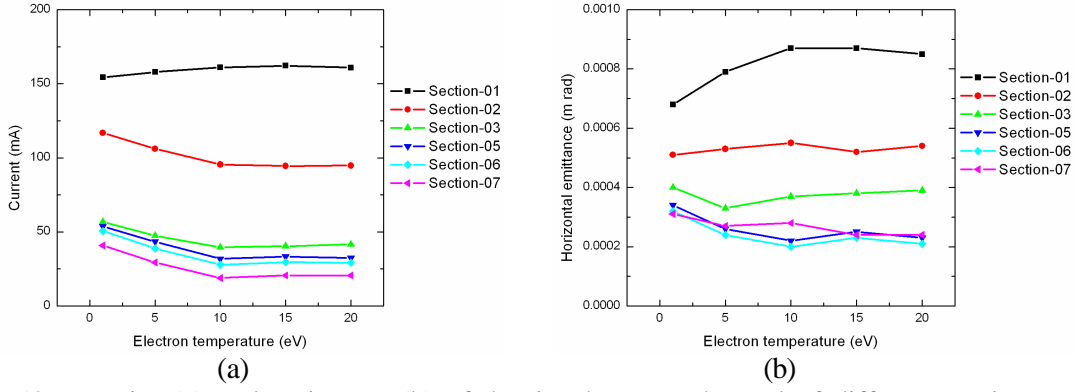
Fig.12 Intensity (a) and emittance (b) of the ion beam at the end of different sections as a function of the electron temperature

5.1.2 Plasma potential hump

Fig.13 presents the dependence of the intensity and emittance of the ion beam at the end of different sections as a function of the plasma potential hump under the initial conditions of 160 eV longitudinal ion energy, 100 eV transverse ion energy, and 180 mA/cm^2 emission current density. It can be seen that the intensity and emittance of the ion beam are not sensitive to the plasma potential hump as well. The main reasons might be that the ions have higher initial energy which depends on the plasma formation process and that the multi-aperture extraction system is used. This multi-aperture extraction system has a relatively high effective emittance compared to the single aperture. Because of physical reasons a plasma potential hump for MEVVA ion source higher than a few volts are not plausible [12,16,18]. In the following simulation the plasma potential hump is specified to 10 V.
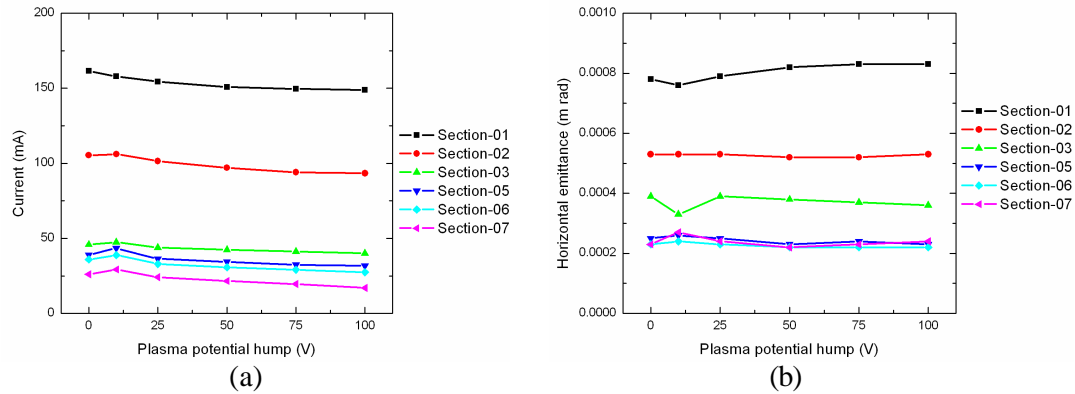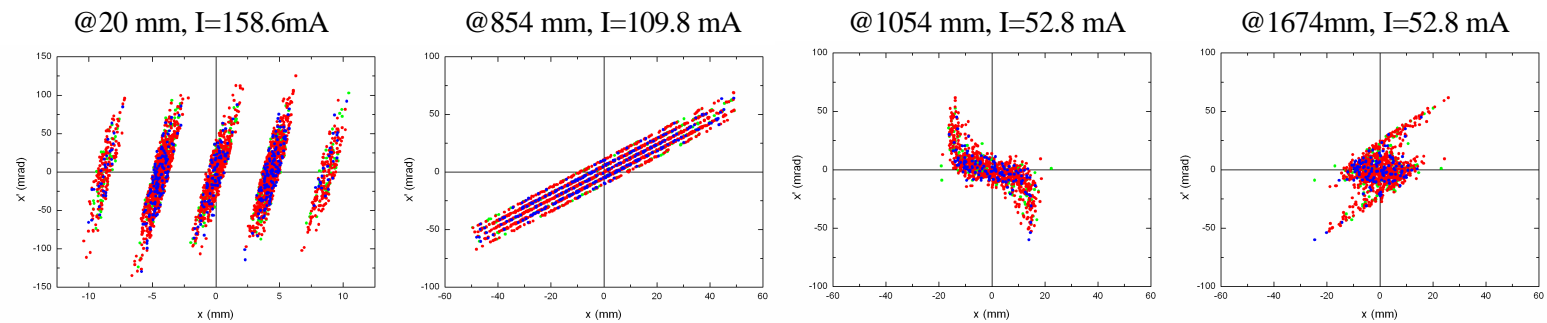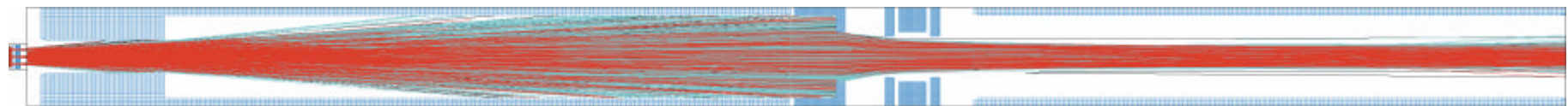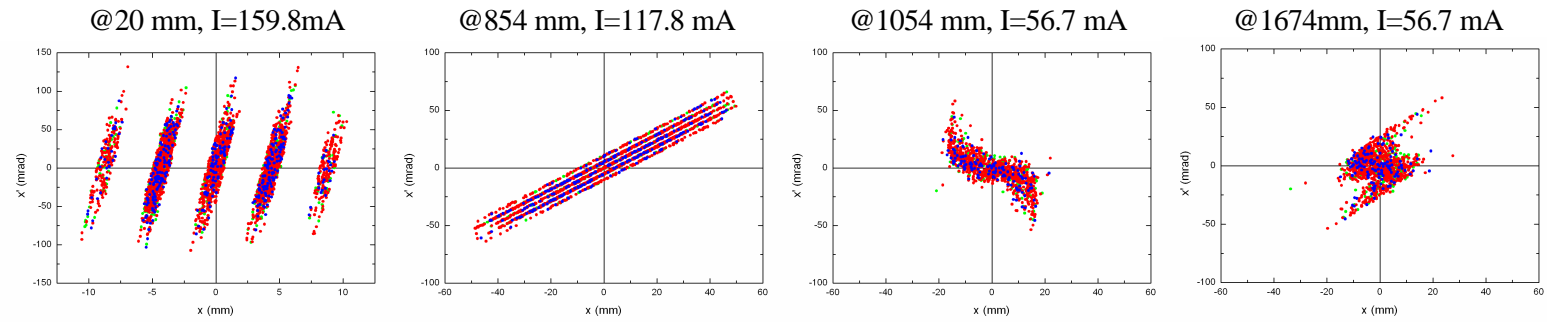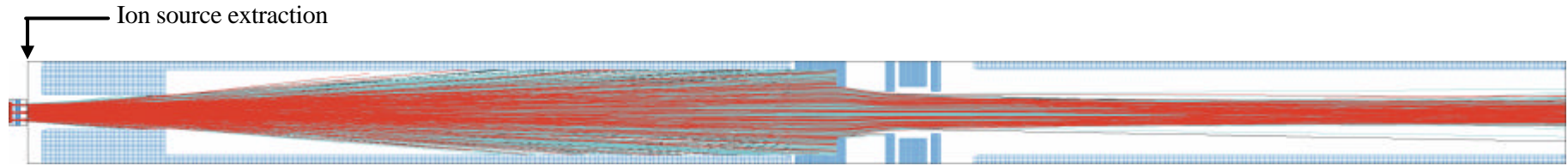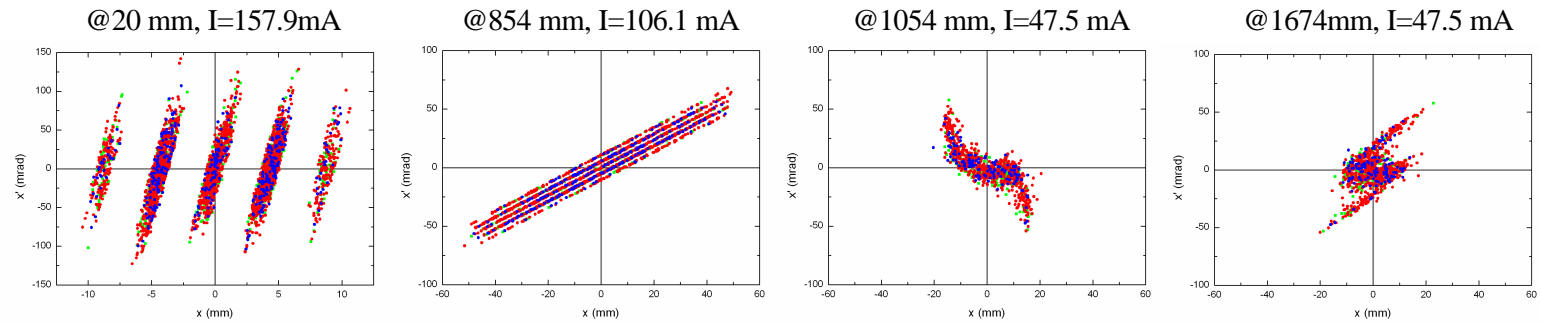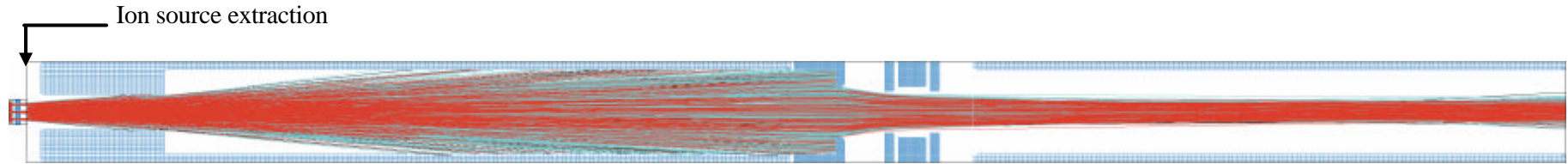

Fig.13 Intensity (a) and emittance (b) of the ion beam at the end of different sections as a function of the plasma potential hump
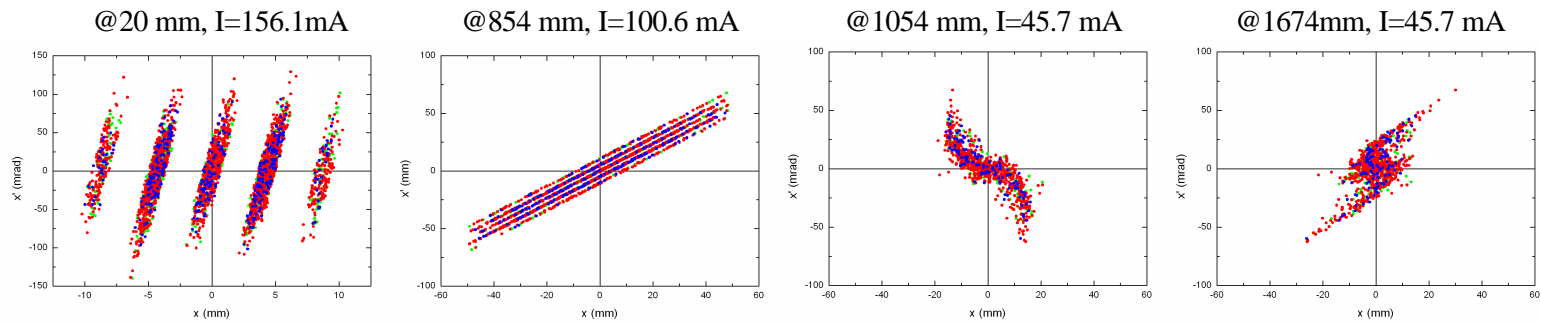
5.1.3 Transverse ion energy

Fig.14 shows the trajectory plots and emittance diagrams for different transverse ion energies with a longitudinal ion energy of 160 eV and an emission current density 180 mA/cm^2. Fig.15 summaries the dependence of the intensity and emittance of the ion beam on the transverse ion energy. It can be seen that the results are not sensitive to the transverse ion energy when the transverse ion energy is up to 10 eV. This phenomenon can be explained by using the same reasons as described above for plasma potential hump. Moreover, when the transverse ion energy is less than 5 eV, there has a notable influence on the intensity and emittance of the ion beam. From Fig.14, one can note that the reason is that the strong losses of the ion beam occur on the wall of the front part of the first drift section when the transverse ion energy more than 5 eV. Moreover, when the transverse ion energy is less than 5 eV, the emittance of the extracted ion beam is smaller, but that of the ion beam behind the acceleration gap becomes larger due to the post acceleration. According to the experimental data [22], the transverse ion energy is specified to 100 eV in the following simulation.

11

Ion source extraction

@20 mm, I=159.8mA

@854 mm, I=117.8 mA

@1054 mm, I=56.7 mA

@1674mm, I=56.7 mA

(a) 5 eV

@20 mm, I=158.6mA

@854 mm, I=109.8 mA

@1054 mm, I=52.8 mA

@1674mm, I=52.8 mA

(b) 50 eV

Ion source extraction

@20 mm, I=157.9mA   @854 mm, I=106.1 mA   @1054 mm, I=47.5 mA   @1674mm, I=47.5 mA

(c) 100 eV

@20 mm, I=156.1mA   @854 mm, I=100.6 mA   @1054 mm, I=45.7 mA   @1674mm, I=45.7 mA
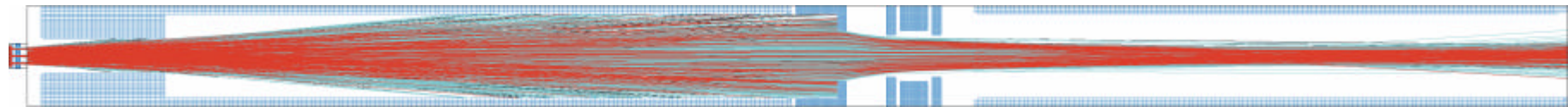
(d) 150 eV

Fig.14 Trajectory plots and corresponding emittance patterns along the beam line for different transverse ion energies.

13

(a)   (b)

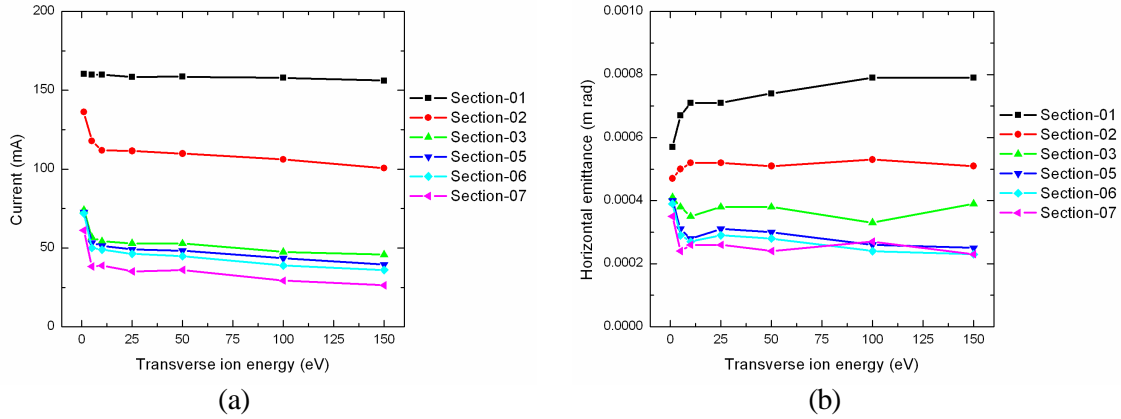Fig.15 Intensity (a) and emittance (b) of the ion beam at the end of different sections as a function of the transverse ion energy

5.1.4 Longitudinal ion energy

Fig.18 and Fig.19 demonstrate the trajectory plots and corresponding emittance patterns along the beam line for different longitudinal ion energies under the initial conditions of 100 eV transverse ion energy, and 180 mA/cm^2 emission current density; the longitudinal ion energy has been varied from 40 to 200 eV. In Fig.16 and Fig.17 the intensity and emittance of the ion beam at the end of different sections as a function of the longitudinal ion energy are demonstrated. One can note that with increasing the longitudinal ion energy the intensity of the ion beam at the end of different sections slightly increases. Moreover, the emittance of the extracted ion beam decreases with increasing the longitudinal ion energy, but there is only a weak influence on those of the ion beam behind the first drift section.
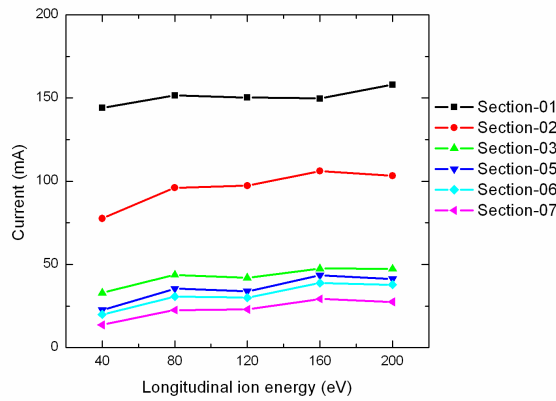
Fig.16 Intensity of the ion beam at the end of different sections as a function of the longitudinal ion energy

Fig.17 Emittance of the ion beam at the end of different sections as a function of the longitudinal ion energy.

14

Ion source extraction

(a) 40 eV

(b) 80 eV

(c) 120 eV

(d) 160 eV

(e) 200 eV
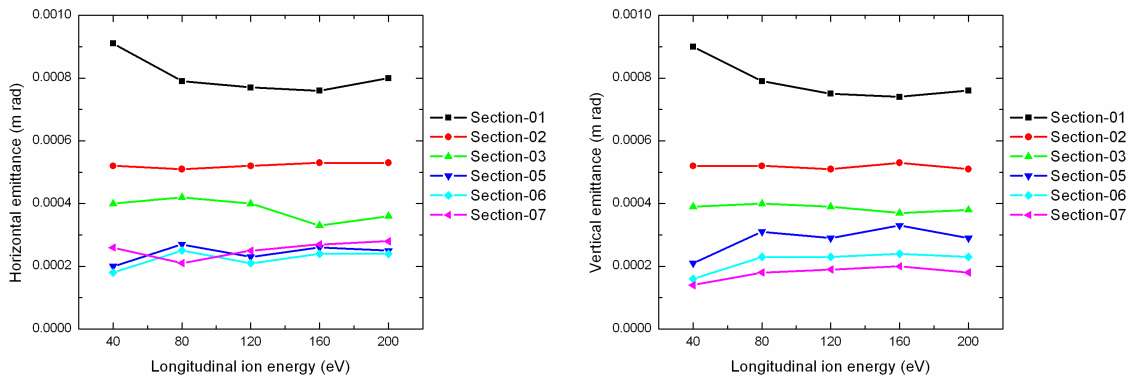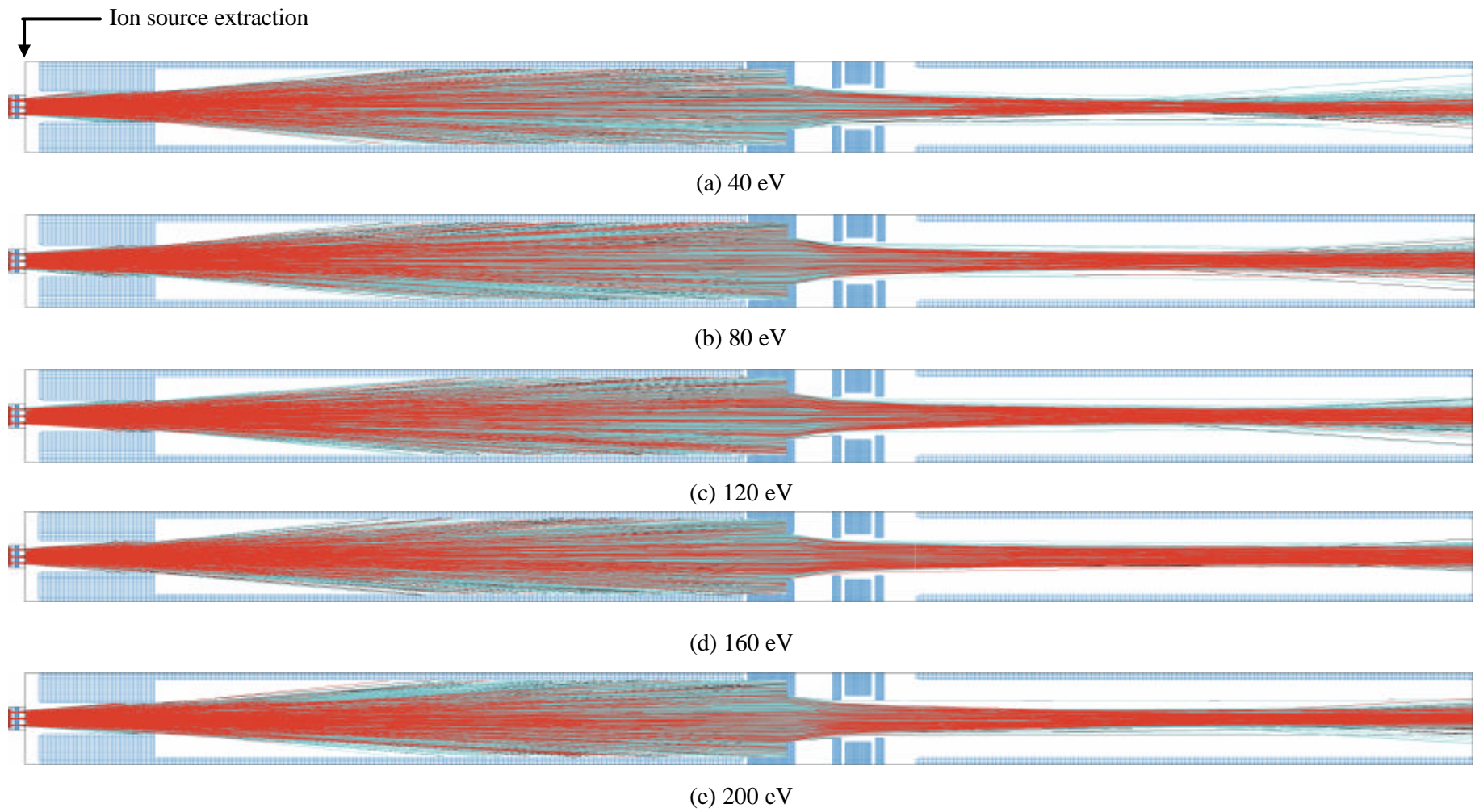
Fig.18 Trajectory plots for different longitudinal ion energies.
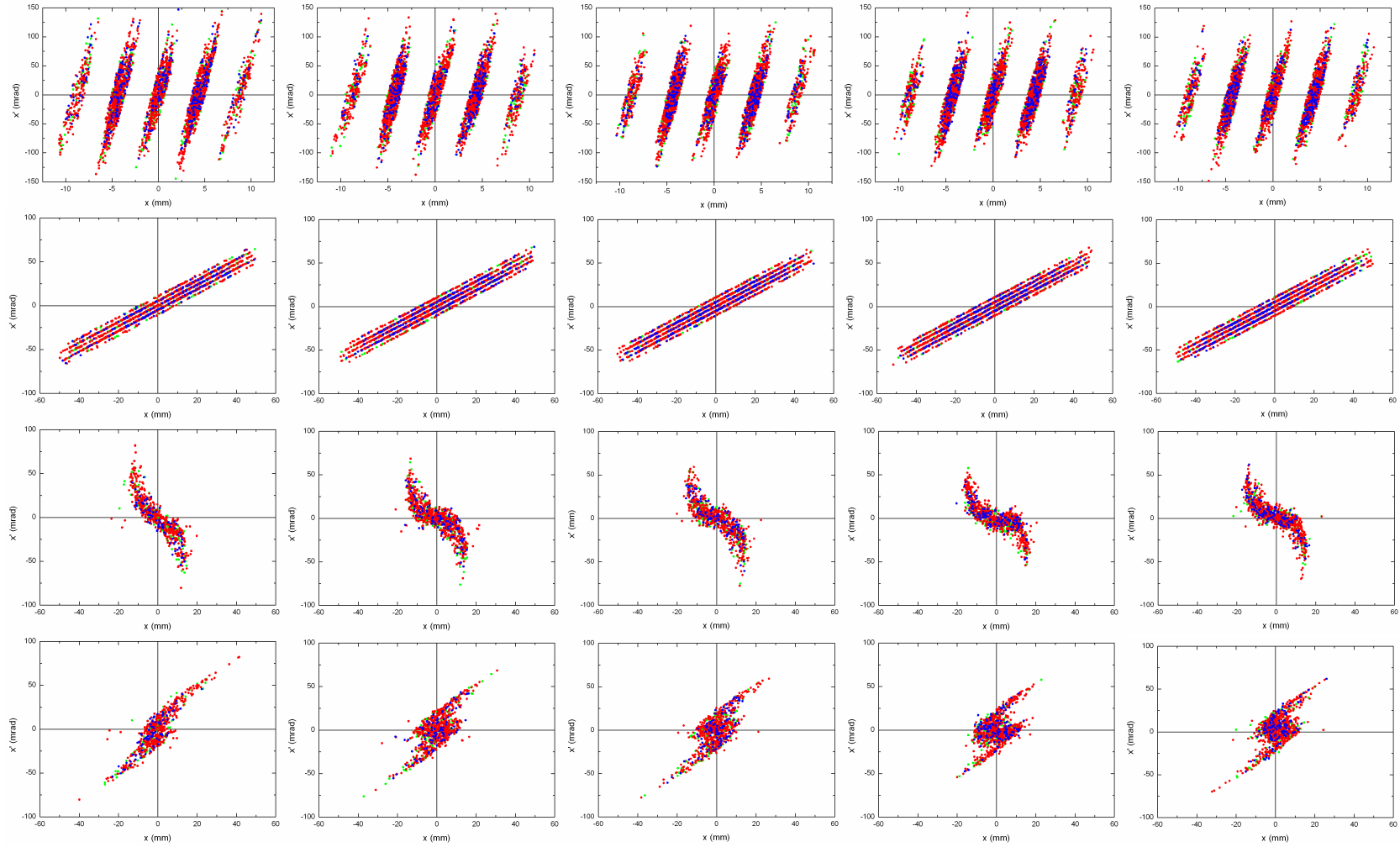
Fig.19 Emittance patterns at the end of different sections for different longitudinal ion energies. From top to bottom: extraction section, first drift section, post-acceleration system, and second drift section. From left to right: 40 eV, 80 eV, 120 eV, 160 eV, and 200 eV.

5.1.5 Emission current density

Fig.20 shows trajectory plots in the extraction system and Fig.22 demonstrates the trajectory plots before the quadrupoles for the emission current density varied from 110 to 270 mA/cm^2 with a 160 eV longitudinal ion energy and 100 eV transverse ion energy. In Fig.23, emittance patterns of the ion beam at the different positions along the beam line are shown. Fig.21 and Fig.25 summarize the intensity and emittance of the ion beam at the end of different sections as a function of the emission current density. From these figures, we may note that there exists a minimum divergence for the extracted ion beam at the emission current density of about 190 mA/cm^2, which corresponds to the perveance matched condition, whereas there is only a slight influence on the emittance of the ion beam behind the acceleration gap. Furthermore, as the emission current density increases, the intensity of the extracted ion beam increases, but the intensities of the ion beam at the end of the other sections do not obey this law. From above figures, it can be easily seen that the losses of the extracted ion beam mainly occur in the first drift section. In addition, the intensity of the ion beam behind the acceleration gap is not sensitive to the emission current density in the range of 180 to 230 mA/cm^2. However, when the emission current density is up to 230 mA/cm^2, the intensities of the ion beam behind the first drift section decreases due to the losses of the ion beam in the first drift section.

If the experimental data with an extracted current of about 135-140 mA and an accelerated fraction of the total current of 45-50 mA are used (see Tab.3), the experimental data can be reproduced in the simulation with the longitudinal ion energy of 188 eV, the transverse ion energy of 100 eV, and the emission current density of 165 mA/cm^2 under the assumption of the full space charge compensation from the screening electrode to the entrance of the acceleration gap, i.e. the simulation is in good agreement with the experimental data. Fig.24 shows the cross-sectional layouts of the beam line together with trajectories produced by simulation, as well as the real space profiles and the emittance patterns of the ion beam along the beam line.

(a)   (b)   (c)   (d)   (e)
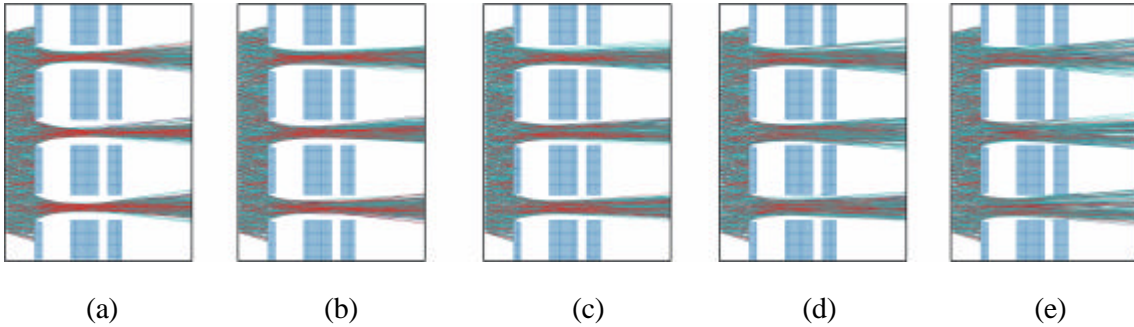
Fig.20 Trajectory plots for different emission current densities and corresponding full beam current in extraction system. (a) 110 mA/cm^2 (102 mA), (b) 150 mA/cm^2 (135 mA), (c) 190 mA/cm^2 (166 mA), (d) 230 mA/cm^2 (194 mA), (e) 270 mA/cm^2 (225 mA)
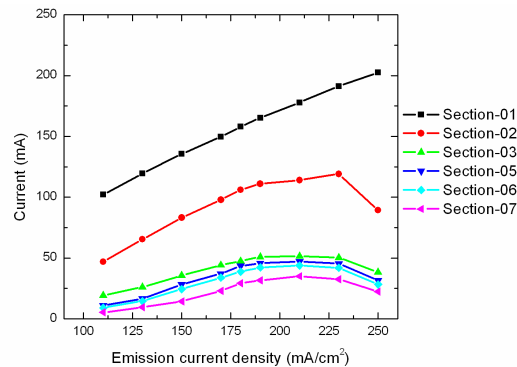
Fig.21 Intensity of the ion beam at the end of different sections as a function of the emission current density

Ion source extraction

(a) 110 mA/cm^2

(b) 150 mA/cm^2

(c) 190 mA/cm^2

(d) 230 mA/cm^2

(e) 270 mA/cm^2
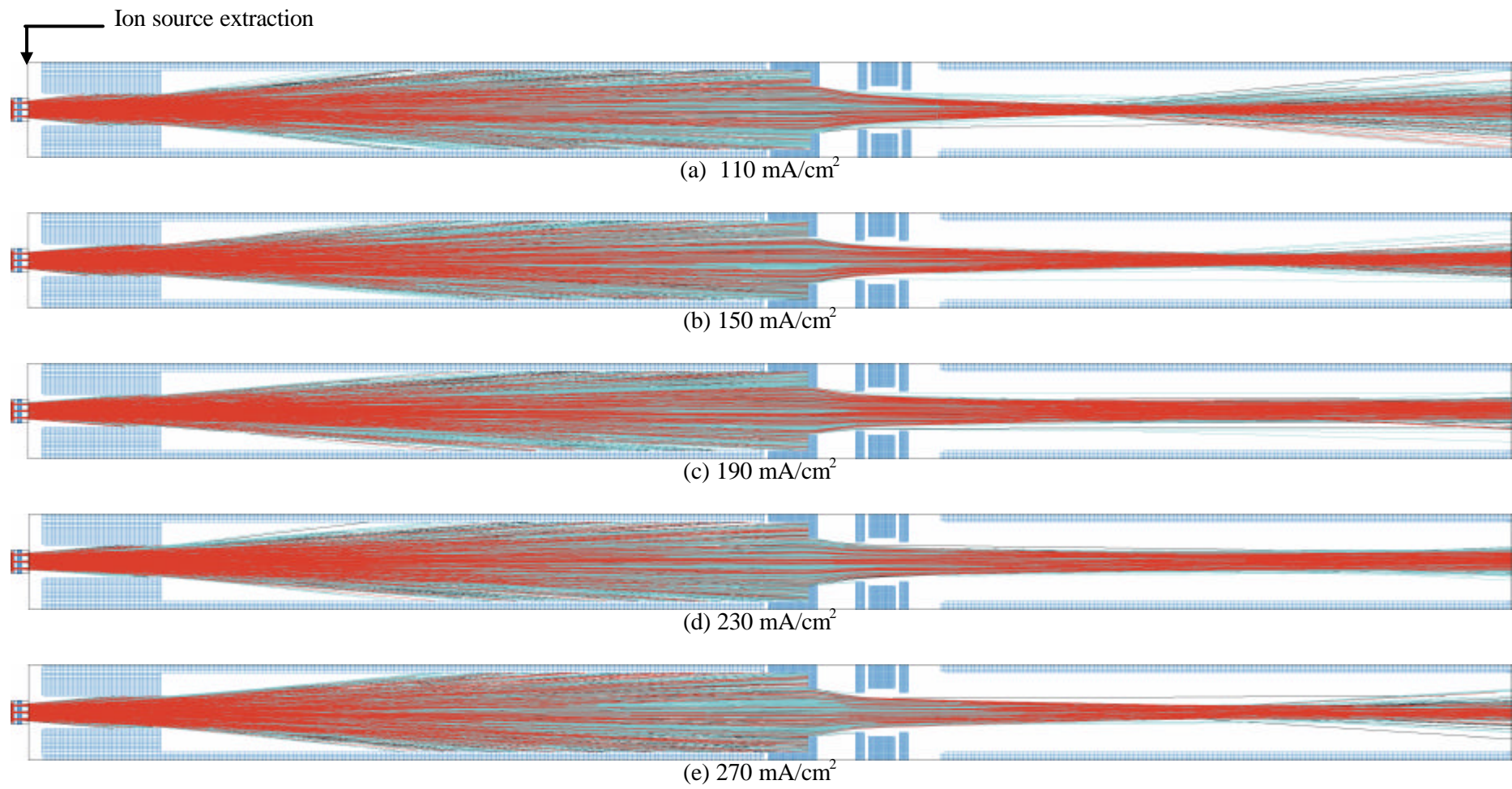
Fig.22 Trajectory plots for different emission current densities.
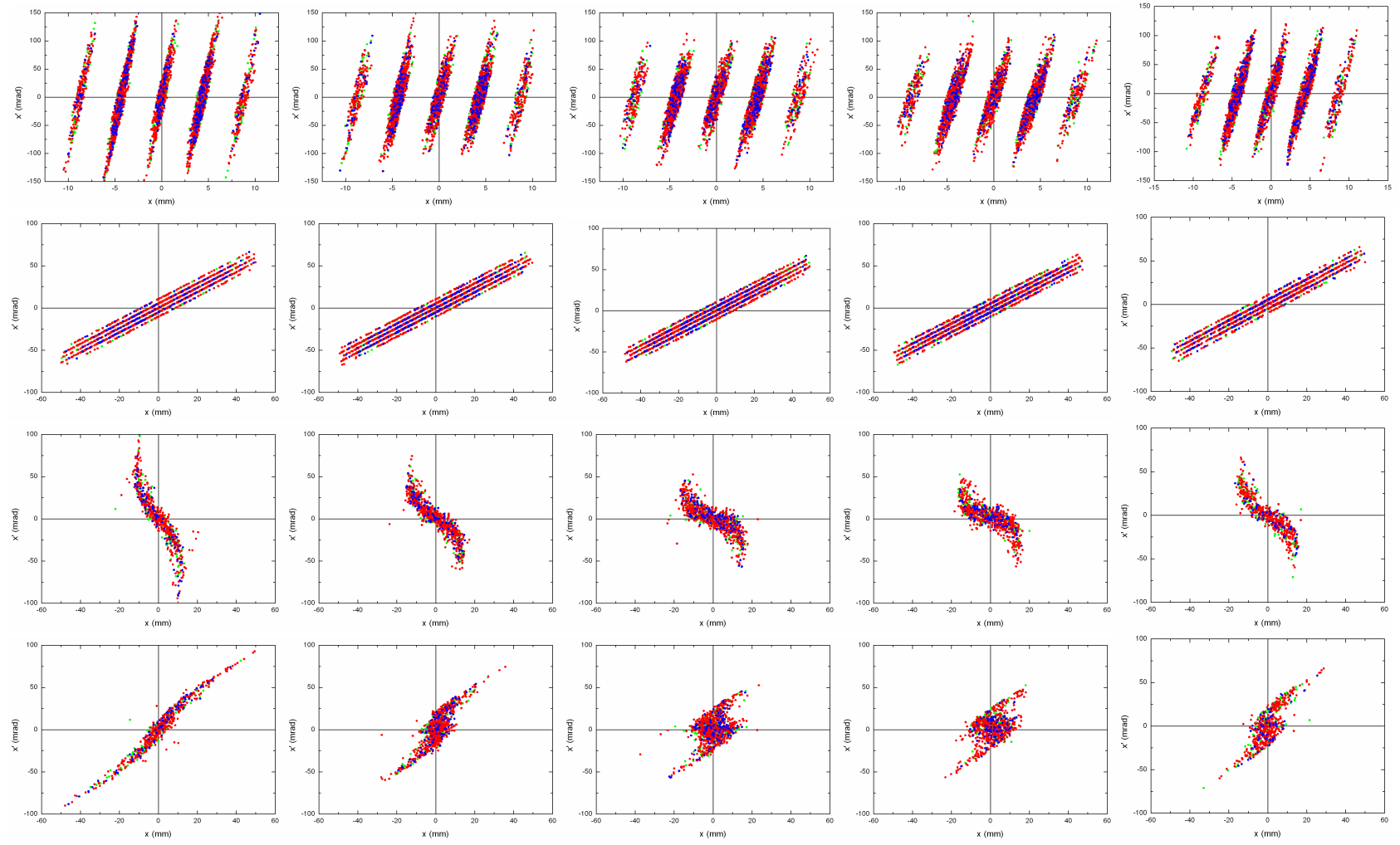
Fig.23 Emittance patterns at the end of different sections for different emission current densities. From top to bottom: extraction section, first drift section, acceleration gap, and second drift section. From left to right: 110, 150, 190, 230, and 270 mA/cm^2.

Longitudinal ion energy: 188 eV;   Transverse ion energy: 100 eV;
Emission current density: 165 mA/cm^2;   Plasma potential hump: 10 V.

(a)
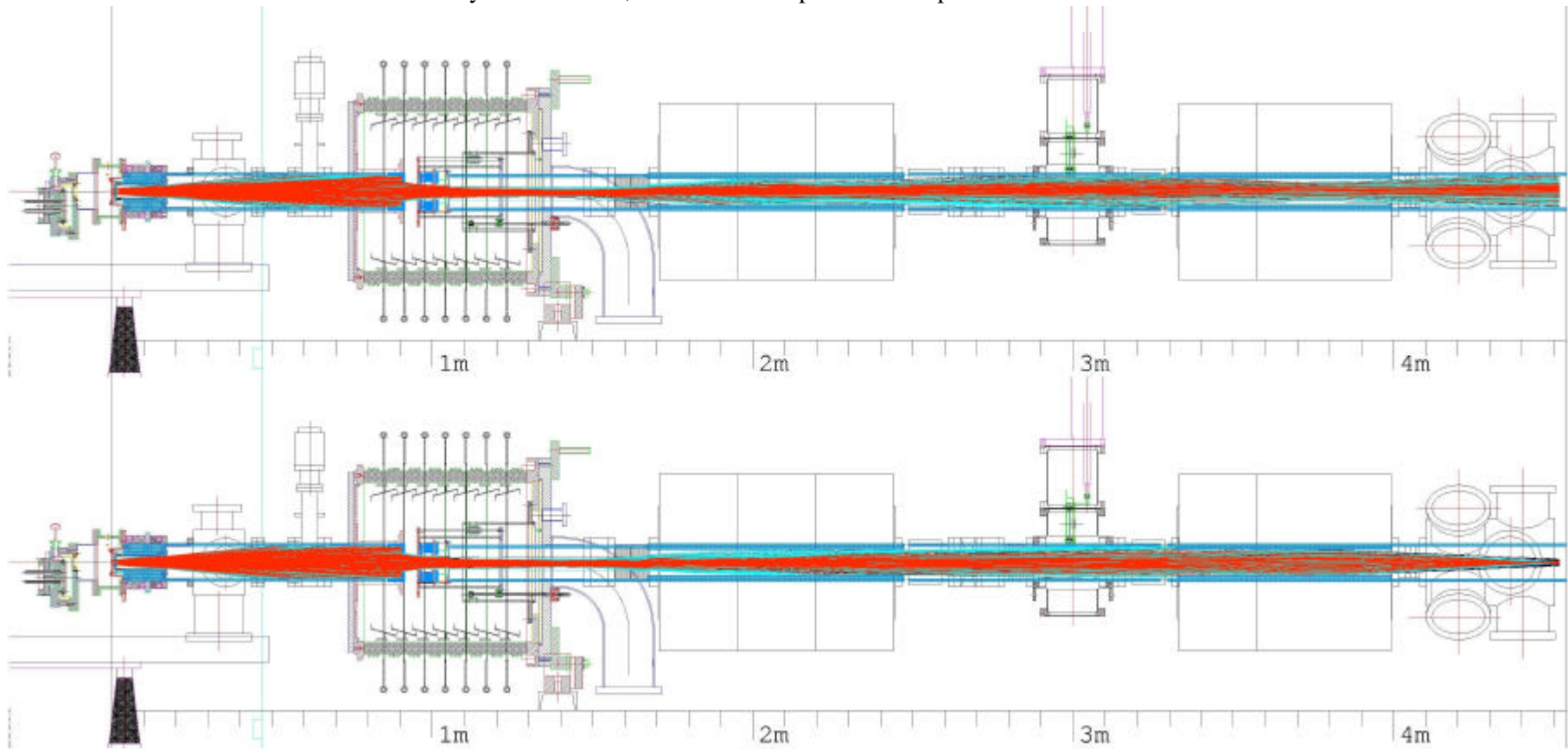
@20 mm	@320 mm	@854 mm	@1054 mm	@1674 mm	@2474 mm	@3294 mm	@4495 mm
I=147mA	I=140.7mA	I=97.9mA	I=45mA	I=45 mA	I=38.5mA	I=35.4mA	I=24.7mA
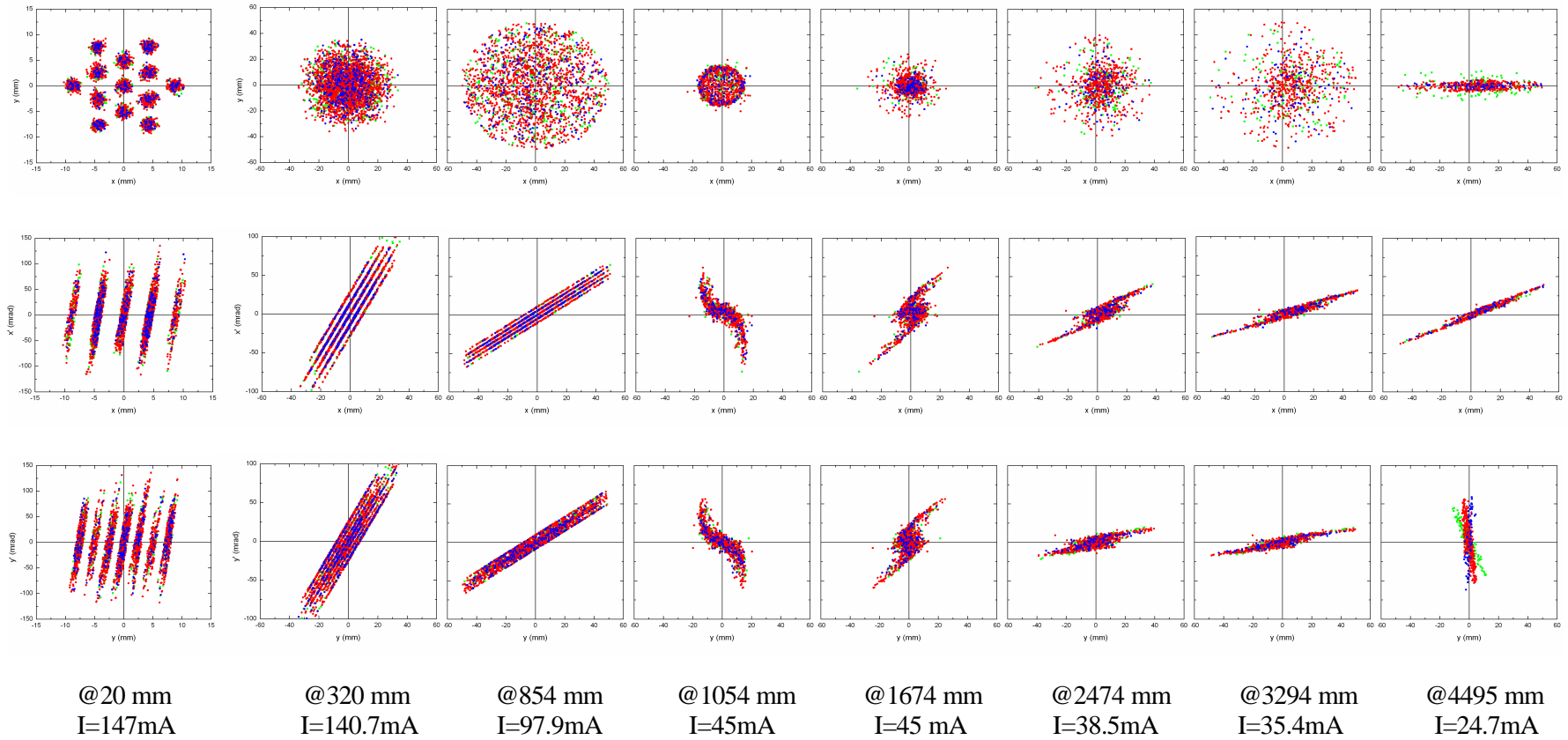
(b)

Fig.24 Cross-sectional layout of the beam line together with trajectories (a), real space profiles and emittance patterns of the ion beam along the beam line (b).
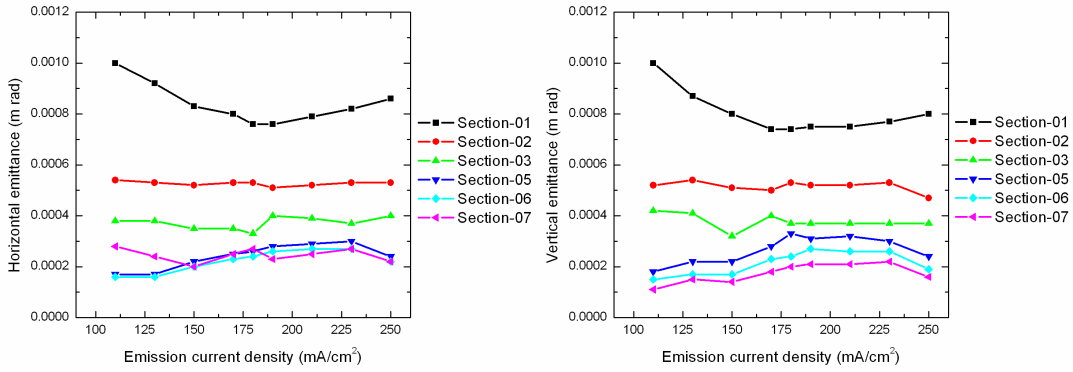
Fig.25 Emittance of the ion beam at the end of different sections as a function of the emission current density

5.2 Simulation on different extraction systems

Fig.26 shows the cross-sectional view of two different extraction systems and potentials applied. They have different thicknesses of the screening electrodes. Fig.27 shows the intensity and emittance of the ion beam extracted from two systems for the longitudinal ion energy of 160 eV, the transverse ion energy of 100 eV, and the emission current density varied from 110 to 270 mA/cm^2. We can easily find that geometry B is more suitable for delivering an ion beam at higher emission current density, with lower beam emittance.

Fig 26 Cross-sectional view of two different extraction systems and potentials applied.PE, plasma electrode; SE, screening electrode; GND, ground electrode.

Fig.27 Intensity (a) and emittance (b) of the extracted ion beam for two different extraction systems as a function of the emission current density

Because the plasma electrode is used to determine the size and shape of the emission aperture and to determine the circum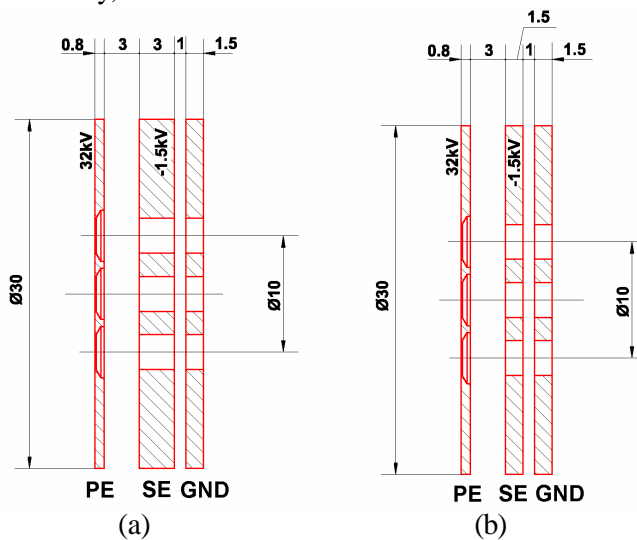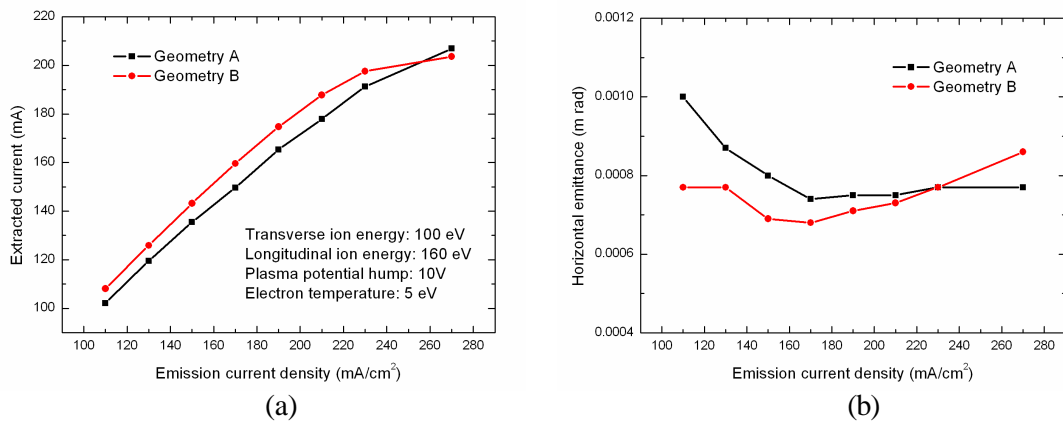ference of plasma meniscus, simulation on the effect of three different aperture shapes as shown in Fig.28 also has been done under the initial conditions of 160 eV longitudinal ion energy, 100 eV transverse ion energy, and 180 mA/cm^2 emission current density. Data comparison is listed in Tab.4. One can note that the simulation confirms that the shape of the apertures plays an important role in the beam formation [27]. The plasma boundary is also shown in Fig.28. The action of the boundary: for shape A, current is too small to fix the boundary to the edge; for shape B the location of the plasma boundary will change while current density fluctuates; for shape C, the plasma boundary is fixed to the edge. One also can find that shape A can be used to extract an ion beam with the highest current but also with highest emittance. Shape B has the lowest current but easiest production. Shape C can deliver an ion beam with the best emittance.
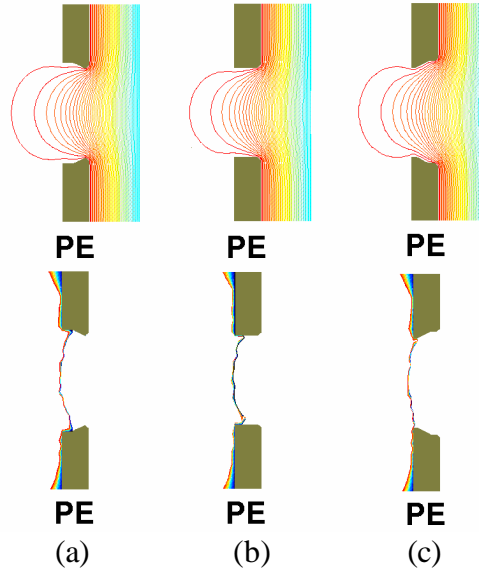
Fig.28 Aperture shapes for the plasma electrode and plasma boundaries. (a) aperture opening toward the source plasma; (b) Cylindrical bore; (c) Aperture opening away from the source plasma. Top: Equipotential plot from Laplace equation; Buttom: plasma boundary. PE, plasma electrode.

Tab.4 Effects of aperture shape of the plasma electrode on the extracted ion beam

Aperture shape	A	B	C
Current(mA)	174.9	150.7	162.8
$e_{x\,rms}$(mm mrad)	780	790	740
$e_{y\,rms}$ (mm mrad)	790	780	760
Features	Highest current	Lowest current	Best emittance

Because the ion current is mainly determined by the extraction area, the influence of the total extraction area on the beam characteristic is also simulated with identical starting conditions (160eV longitudinal ion energy, 100 eV transverse ion energy, 180 mA/cm^2 emission current density and 10 V plasma potential hump). Fig.29 shows the geometries of two extraction systems with different numbers of extraction holes. Data comparison is summarized in Tab.5. One can note that the 19-hole extraction system increases the total extraction area by 46% compared to 13-hole extraction system. The intensities of the extracted ion beam and accelerated ion beam are increased by 49% and 27%, respectively. Fig.30 shows the emittance diagrams after extraction and after acceleration for two different extraction areas. It can be seen that the accelerated ion beam for both extraction systems has similar divergence and emittance. This increase of the extracted ion beam current without modifying the x-x' and y-y' emittance by increasing the transmission can possibly explained by the specific projections of the four dimensional phase space into a 2D space.
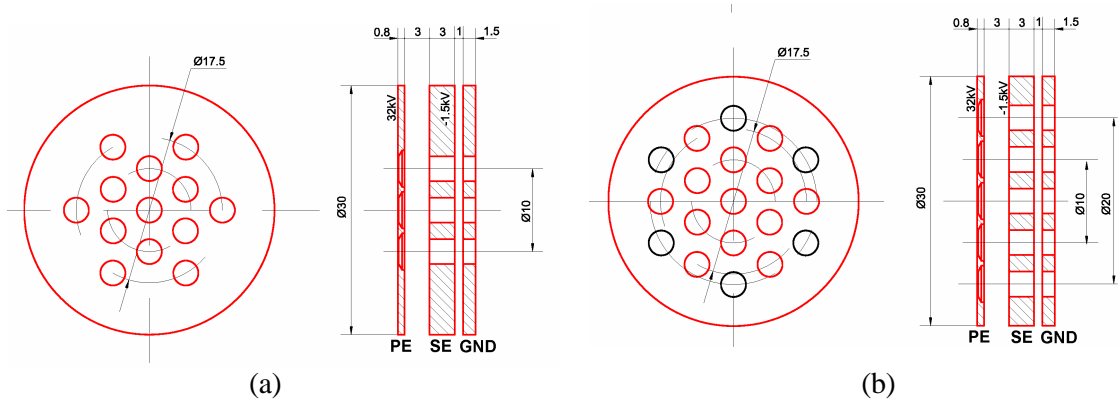
Fig.29 Geometries of the extraction system with 13-hole (a) and with 19-hole (b). PE, plasma electrode; SE, screening electrode; GND, ground electrode.

Tab.5 Effects of the total extraction area

	Total area (cm²)	Extracted current (mA)	Accelerated current (mA)
13 holes	0.919	157.9	47.5
19 holes	1.343	235.5	60.3
Increase	46%	49%	27%

(a) 13 holes   (b) 19 holes
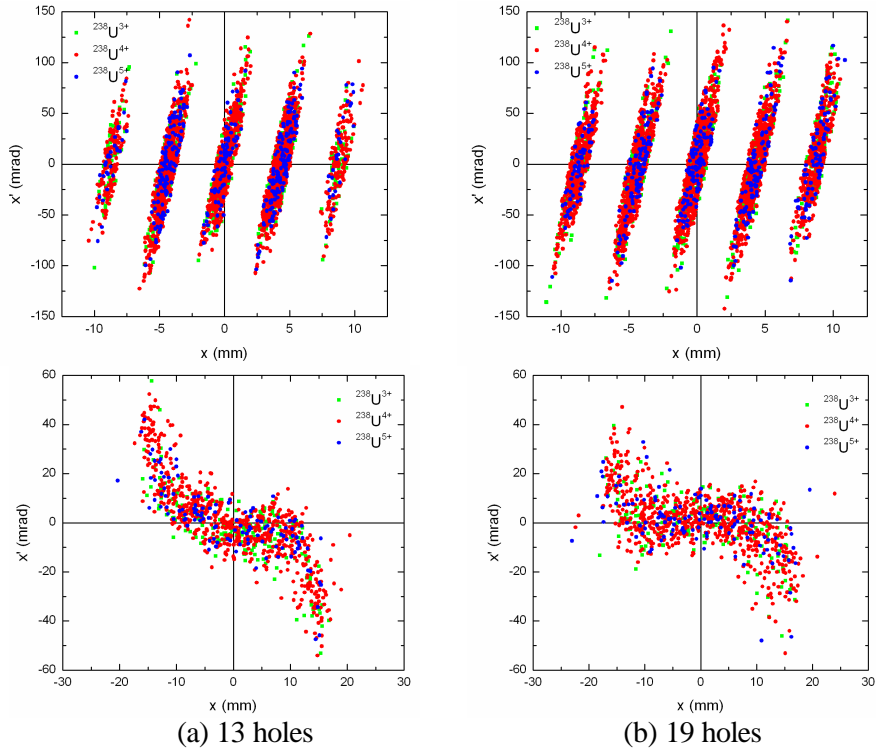
Fig.30 Beam emittance diagrams for a 13-hole extraction system (a) and a 19-hole extraction system (b) after extraction (top) and after acceleration (bottom)

5.3 Simulation on the acceleration gap

In order to optimize the acceleration gap, six different geometries for the acceleration gap as shown in Fig.32 are used to investigate the effect of geometries of the acceleration gap on the accelerated ion beam quality under the conditions of equal intensity, profile and divergence of the extracted ion beam. Fig.31 and Fig.33 show the intensity and emittance of different geometries for an extracted ion beam current of 115 mA. One can find that, compared to the standard geometry, the other geometries can be used to reduce the divergence of the accelerated

24

ion beam in a certain extent. Geometry C has the largest current, but geometries D, E and F have the lowest divergence. That the same intensity and the emittance of the extracted ion beam for geometries D, E and F indicates that the extracted ion beam quality is not sensitive to the slant distance of the high voltage electrode. To find all dependencies more systematically several parameters have been varied while keeping all other conditions constant in the following simulation.
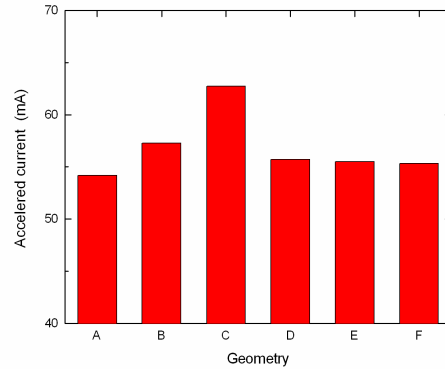
Fig.31 The dependence of accelerated ion beam current on different geometries of the acceleration gap
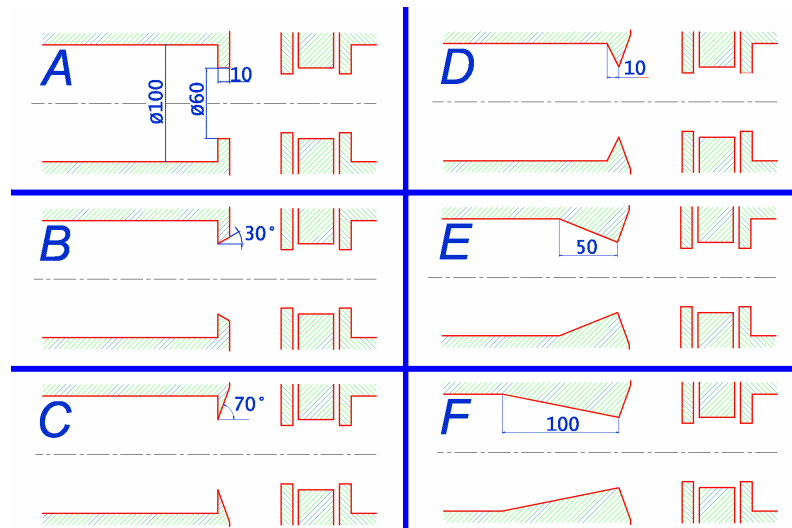
Fig.32 Different geometries of the acceleration gap. A, standard geometry; B, high voltage electrode with 30°; C, high voltage electrode with 70° ; D, E, and F high voltage electrode with 70° and different slant distances.
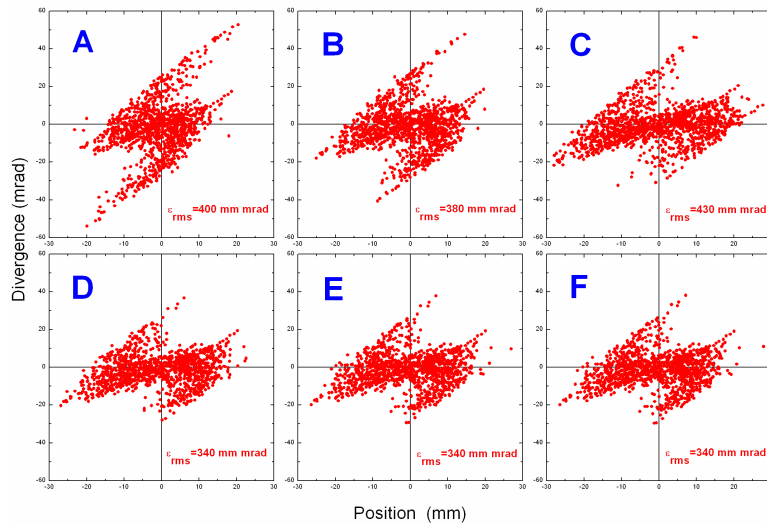
Fig.33 Beam emittance diagrams of the accelerated ion beam for different geometries

First the optical properties of the acceleration gap have been investigated. The effects of the intensity and emittance of the extracted ion beam with respect to geometry D were simulated. Fig.34 shows the influence of the emittance of the extracted ion beam varied from 480 to 2700 mm mrad on the ion trajectories, the beam profiles and the emittance diagrams before and after acceleration. It should be pointed out that the five diagrams of the extracted ion beam at the bottom in Fig.34 are produced from the upper one. The intensity and profile of the extracted ion beam have been kept constant in the simulation. One can note that the top acceleration gap can be used to produce a focused beam, whereas the others are divergent. From Fig.35, it can be seen that the intensity of the accelerated ion beam and transmission of the gap are inversely proportional to the emittance of the extracted ion beam. The transmission of the gap is always less than 50%.
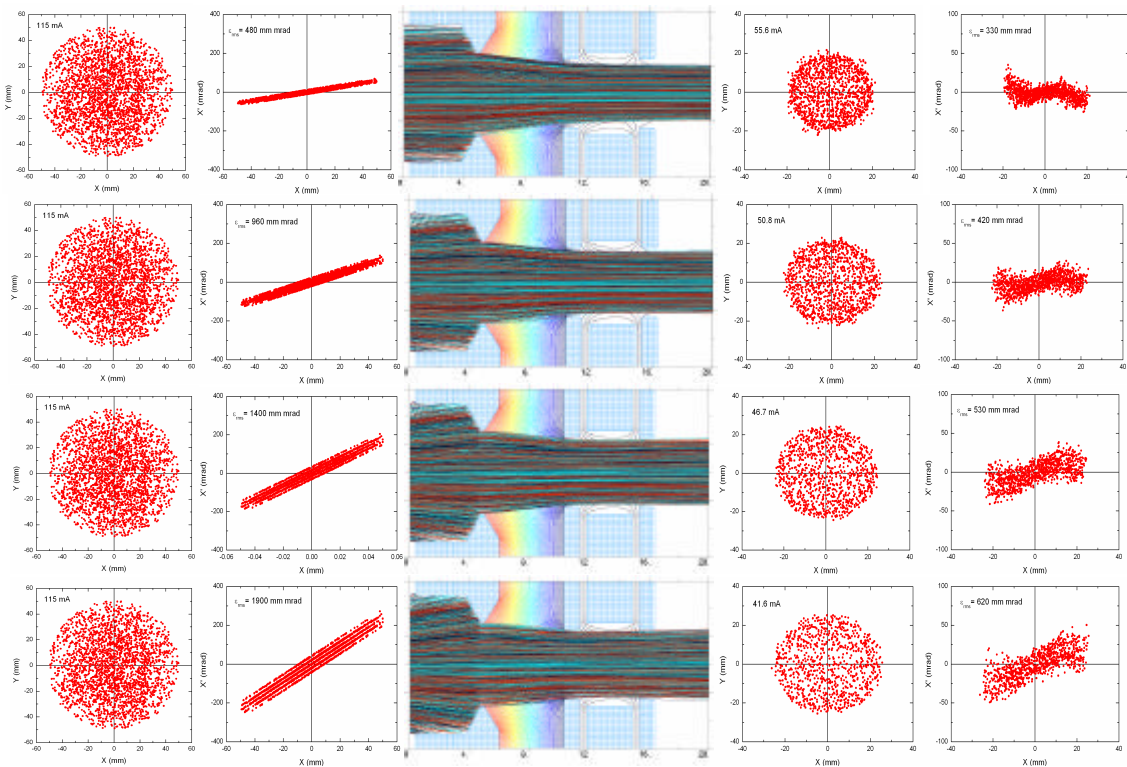
Fig.34 Trajectory plots, beam profiles, and emittance diagrams for different emittances of the extracted ion beam. From left to right, real space and emittance diagram of the extracted ion beam, trajectory plot, real space and emittance diagram of the accelerated ion beam. From top to bottom, emittance of the extracted ion beam are: 480, 960, 1400, 1900, 2300, and 2700 mm mrad, respectively.

(a)

(b)

(c)
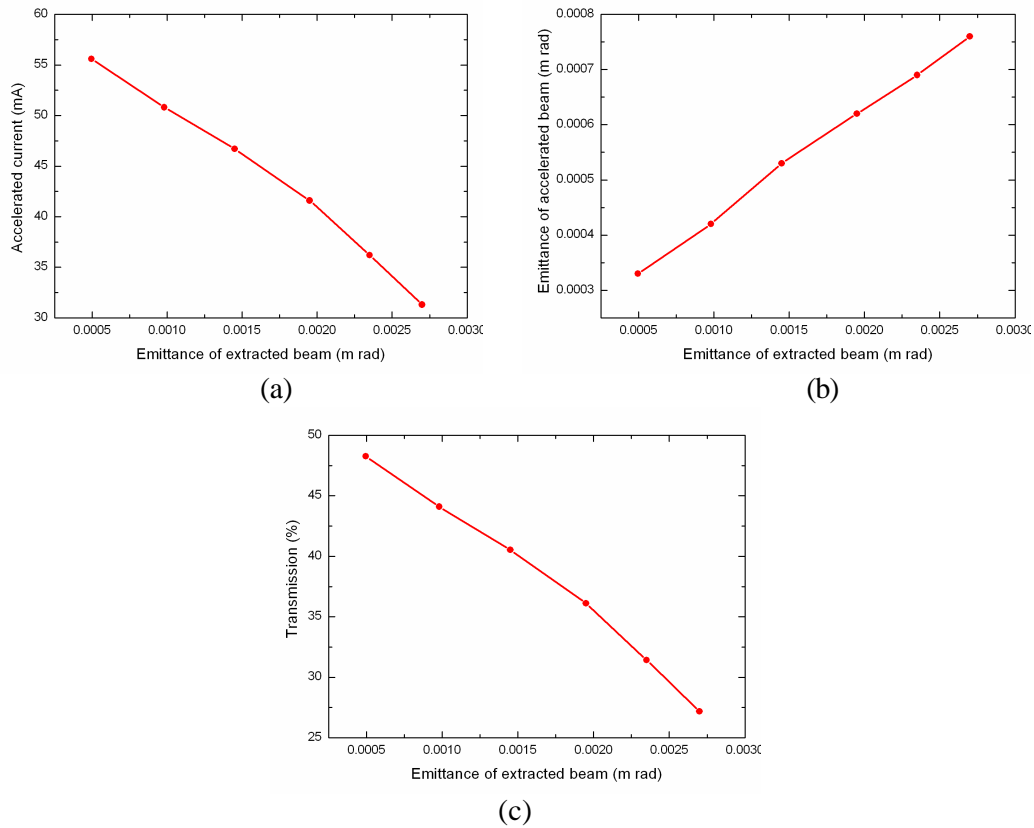
Fig.35 Intensity (a), emittance (b), and transmission (c) of the accelerated ion beam as a function of the emittance of the extracted ion beam.

Simulation also was done with the total extracted current varied from 115 to 346 mA but with the same emittance and the same profile of the extracted ion beam. The relevant results are shown Fig.36, Fig.37, Fig.38, and Fig.39. From these figures, we may find that, with increasing the intensity of the extracted ion beam, both the intensity and emittance of the accelerated ion beam increase. The intensity of the accelerated ion beam is directly proportional to that of the extracted ion beam when the extracted ion beam current is less than 230 mA, however the accelerated ion beam current stays constant when the extracted ion beam current is up to 300 mA, i.e. the intensity of the accelerated ion beam reaches a saturating value. With increasing the intensity of the extracted ion beam the transmission of the gap decreases. When the extracted

ion beam current is up to 230 mA, the transmission of the gap decreases rapidly. Furthermore, the transmission of the gap is also less than 50%. With increasing the intensity of the extracted ion beam from 115 to 346 mA the ellipse acceptance area of the accelerated ion beam increases from 14 to 25 cm^2; the emittance of the accelerated ion beam increases from 330 to 480 mm mrad, and corresponding maximum and minimum divergence of the accelerated ion beam varies from 35 to 67 mrad and from -26 to -80 mrad, respectively.

Fig.40 shows the dependence of the intensity and emittance of the accelerated ion beam as a function of the acceleration gap width for the extracted current of 115 mA and the emittance of 480 mm mrad. One can find that with increasing the gap width from 30 to 60 mm the intensity and emittance of the accelerated ion beam decrease from 56 mA and 400 mm mrad to 55 mA and 300 mm mrad, respectively.

The focusing strength of the gap will be increased by reducing the gap width. Image errors (aberrations) due to the non-ideal aspect ratio will increase the emittance on the other hand. An optimum gap width is therefore expected for each actual set of parameters.
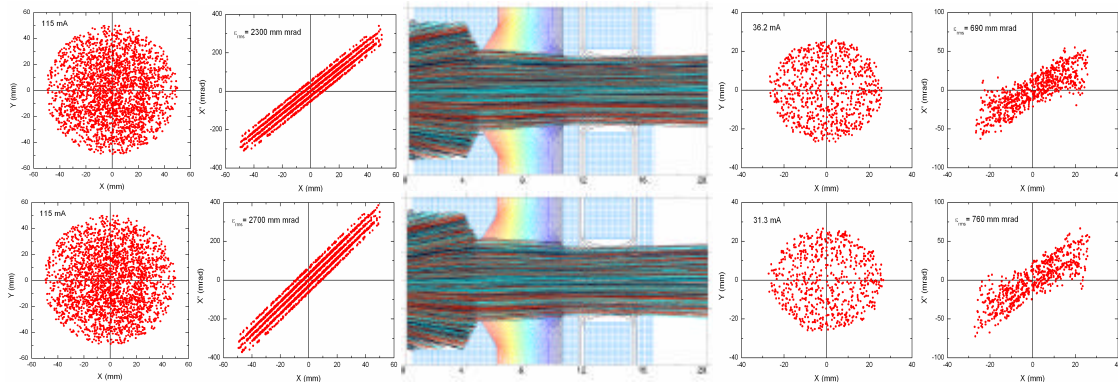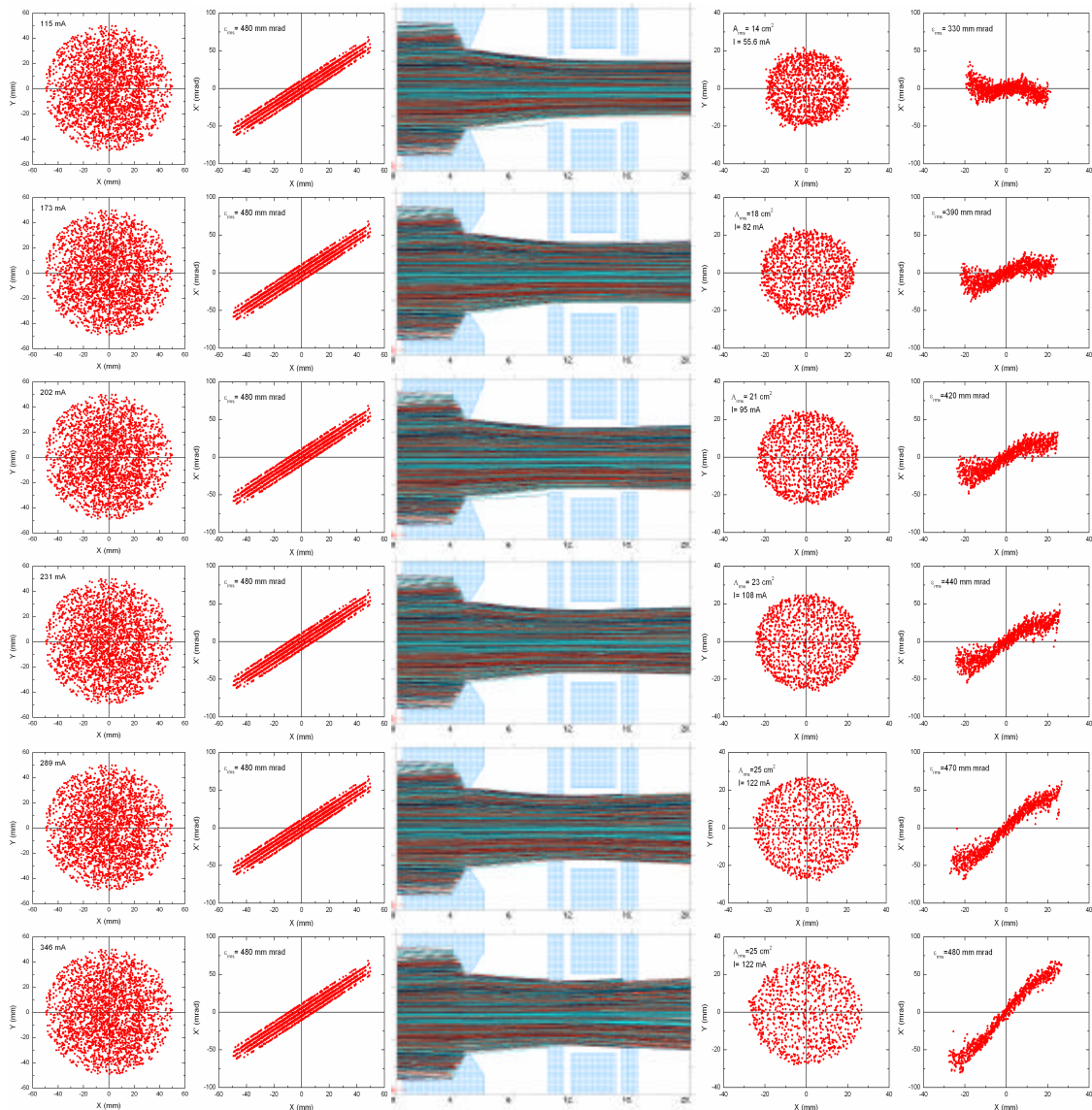

Fig.36 Trajectory plots, beam profiles, and emittance diagrams for the different extracted ion beam current. From left to right, real space and emittance diagram of the extracted ion beam, trajectory plot, real space and emittance diagram of the accelerated ion beam. From top to bottom, 115, 173, 202, 231, 289, and 345 mA, respectively

<div align="center">(a)</div> <div align="center">(b)</div>
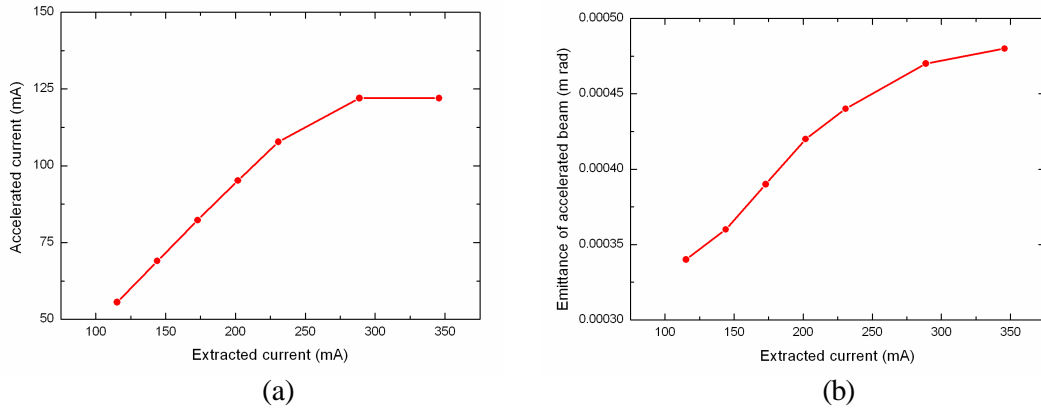
Fig.37 Intensity (a) and emittance (b) of the accelerated ion beam as a function of the extracted ion beam current.
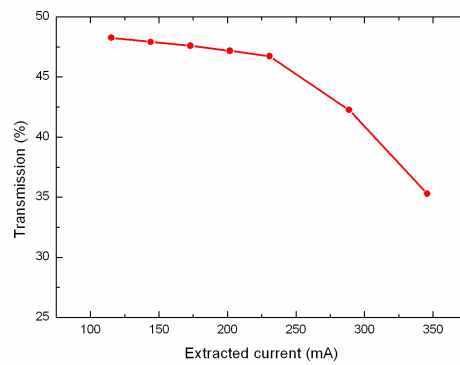
Fig.38 Transmission of the accelerated ion beam as a function of the extracted ion beam current.
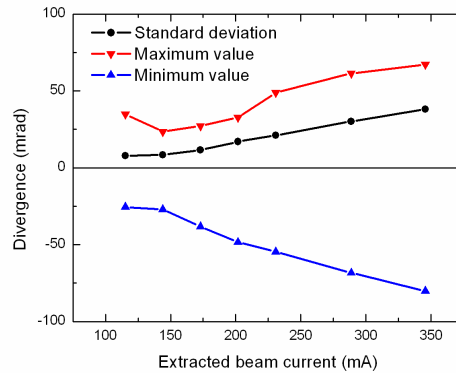
Fig. 39 Divergence of the accelerated ion beam as a function of the extracted ion beam current.

<div align="center">(a)</div> <div align="center">(b)</div>
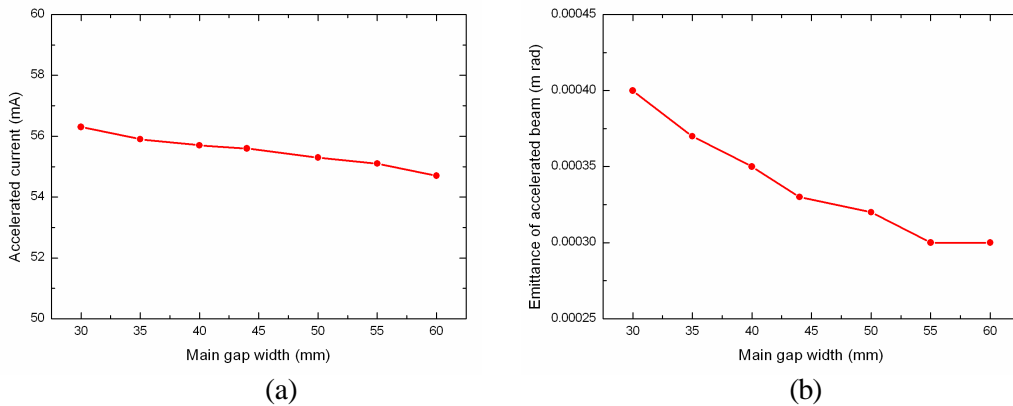
Fig.40 Intensity(a) and emittance(b) of the accelerated ion beam as a function of the acceleration gap width.

6. Conclusion

The characteristics of the ion beam extracted from one of the GSI high current ion sources MEVVA and VARIS in the injection beam line for the UNILAC was investigated by using the KOBRA3-INP code. The results show that the losses of the extracted ion beam propagating through the beam line mainly occur in the drift space between the extraction system and the acceleration gap. The intensity of the ion beam behind the acceleration gap is not sensitive to the emission current density in the range 180 to 230 mA/cm^2. Simulation also indicates that one of the extraction systems is suitable for delivering an ion beam at higher emission current density, with lower beam emittance; and a 19-hole extraction system might be used to increase the intensity of the delivered ion beam compared to the regularly used 13-hole extraction system. Simulation also confirms that the shape of the aperture plays an important role in the beam formation. Simulation quantitatively supports the experimental results under the assumption that the ion beam is space charge compensated along the drift sections; otherwise the transport would not be possible. Moreover, the understanding obtained through this work will provide the basis for optimizing the extraction system and the acceleration gap for the ion source.

References

[1] I.G. Brown, J.E. Galvin, B.F. Gavin, and R.A. MacGill, Metal vapor vacuum arc ion source, Rev. Sci. Instrum. 57 (6), 1069 (1986).

[2] I.G. Brown, B. Feinberg, and J.E. Galvin, Multiply stripped ion generation in the metal vapor vacuum arc, J. Appl. Phys. 63, 4889 (1988).

[3] I.G. Brown, J.E. Galvin, R. Keller, P. Spädtke, R.W. Müller, and J. Bolle, Transport and acceleration of high current uranium ion beams, Nucl. Instr. and Meth. in Phys. Res. A245, 217 (1986).

[4] P. Spädtke, H. Emig, J. Klabunde, D.M. Rück, B.H. Wolf, and I.G. Brown, High current metal ion beam transport in the UNILAC injector at GSI, Nucl. Instr. and Meth. in Phys Res. A278, 643 (1989).

[5] H. Reich, P. Spädtke, and E.M. Oks, Metal vapor vacuum arc ion source development at GSI, Rev, Sci. Instrum. 71 (2), 707 (2000).

[6] M. Galonska, F. Heymach, R. Hollinger, and P. Spädtke, Vacuum arc ion source: Charge state enhancement and arc voltage, In: Emerging applications of vacuum-arc-produced plasma, ion and electron beam. Eds: E. Oks and I.G. Brown. Kluwer Academic Publishers. Dordrecht, 2002, p123-130.

[7] R. Hollinger, F. Heymach, and P. Spädtke, Emittance measurements at the high current injector at GSI, Rev. Sci. Instrum. 73 (2), 1024 (2002).

[8] P. Spädtke, J. Bossler, H. Emig, K.D. Leible, C. Mühle, H. Reich, and H. Schulte, Ion source development at GSI, Rev. Sci. Instrum. 69 (2), 1079 (1998).

[9] E.M. Oks, P. Spädtke, H. Emig, and B.H. Wolf, Ion beam noise reduction method for the MEVVA ion source, Rev. Sci. Instrum. 65 (10), 3109 (1994).

[10] A. Anders, and R. Hollinger, Reducing ion-beam noise of vacuum arc ion sources, Rev. Sci. Instrum. 73 (2), 732 (2002).

[11] P. Spädtke, U^{4+} MEVVA source & outlook for HIF sources, Nucl. Instrum. and Meth. in Phys. Res. A464, 388 (2001).

[12] R. Hollinger, Ion extraction, In: The physics and technology of ion sources, 2nd Edition. Eds: I.G. Brown, Wiley-VCH, Berlin, 2004.

[13] H.S. Zhang, Ion sources, Springer, Berlin, Science Press, Beijing, 1999.

[14] H. Reich, F. Heymach, and P. Spädtke, Commissioning of the high current ion sources at the new GSI injector (HSI), Proc. 20th Inter. Linac Conf. Monterey, CA, 2000, p238-240.

[15] R. Hollinger, M. Galonska, F. Heymach, and P. Spädtke, MEVVA ion source for uranium high current operation at the GSI accelerator facility, Proc. 20th Int. Symp. on Discharge and Electrical Insulation in Vacuum, Tours, France, 2002, p447-450.

[16] R. Hollinger, M. Galonska, and P. Spädtke, Development of a vacuum arc ion source for injection of high current uranium ion beam into the UNILAC at GSI, Rev. Sci. Instrum. 75 (5), 1595 (2004).

[17] INP, Junkerstr. 99, 65205 Wiesbaden, Germany.

[18] P. Spädtke, Computer simulation of extraction, In: The physics and technology of ion sources, 2nd Edition. Eds: I.G. Brown, Wiley-VCH, Berlin, 2004.

[19] U. Ratzinger, Commissioning of the new GSI high current linac and HIF related RF linac aspects, Nucl Instrum. and Meth. in Phys. Res. A464, 636 (2001)

[20] W. Barth, Commissioning of the 1.4 MeV/u high current heavy ion LINAC at GSI, Proc. 20th Inter. Linac Conf., Monterey, CA, 2000, p1033-1137.

[21] P. Spädtke, Simulation of the extraction from a MEVVA ion source, In: Emerging applications of vacuum-arc-produced plasma, ion and electron beam. Eds: E. Oks and I.G. Brown, Kluwer Academic Publishers. Dordrecht, 2002, p67-76.

[22] M. Galonska, R. Hollinger, and P. Spädtke, Charge sensitive evaluated ion and electron energy distributions of a vacuum arc plasma, Rev. Sci. Instrum. 75 (5), 1592 (2004).

[23] S.A. Self, Exact solution of the collisionless plasma-sheath equation, Phys. Fluids, 6 (1963) 1762.

[24] P. Spädtke, H. Emig, J. Klabunde, R. Mayr, D.M. Rück, and K. Tinschert, Acceleration of high-current ion beams, Rev. Sci. Instrum. 67 (3), 1146 (1996).

[25] GSI Technical Report: magnetic field measurement, QSL85, No. 80346 (1999).

[26] GSI Technical Report: magnetic field measurement, QSL85, No. 80362 (1999).

[27] L.R Grisham, C.C Tsai, J.H. Whealton, and W.L. Stirling, Effect of emission aperture shape upon ion optics, Rev. Sci. Instrum. 48 (8), 1037 (1977).

[28] M. Galonska, doctoral thesis: Entwicklung und Untersuchung einer Vakuumbogen-Ionenquelle zur Erzeugung intensiver, hochbrillianter vierfach geladener Uranstrahlen , University of Frankfurt (in preperation).

Appendix

General Remarks

Several simulations have been made in parallel to the writing of this report to investigate the specific influence of starting conditions of the trajectories on the transported beam.

All figures shown here are high quality, very high resolution vector graphic (each figure is in the order of 100 MB). Due to the way of reproduction the quality of resolution is very limited. The original figures can be obtained on request on CD. Contact p.spaedtke@gsi.de to receive a copy.

Starting Conditions of Trajectories

In the simulation, it is necessary to start each trajectory with a certain initial energy. However, it is important to start with the correct values, otherwise unrealistic results are obtained. From theory we are strongly convinced, that the initial energy of ions is given mainly by the explosive character of the discharge, and not by a potential drop between plasma and plasma electrode [28]. Whereas in the second case the velocity depends on the charge state, it is constant in the first case for all charge states before extraction. Nevertheless, we have simulated here the two different options to check the influence of both models on the beam properties: the potential model and the explosive model, both can be simulated with KOBRA3-INP [18]. This initial energy can be defined separately in longitudinal and transverse direction. The longitudinal component of the initial energy has been kept constant with $160 \times q$ [eV] for the potential model, or with a velocity up to $\beta = \frac{v}{c} = 3.8 \cdot 10^{-5}$ for the momentum model, respectively.

In the first section (inside the plasma) always 15.600 trajectories are launched distributed in three charge states: $^{238}U^{3+}$, $^{238}U^{4+}$, $^{238}U^{5+}$. The measured charge state distribution has been taken as reference. Only the transverse component of the initial energy has than be modified, to check its influence.

Because the current per trajectory might be different, the real transmission is listed in the table with the electrical current.

Note, that the electrical current is given in total for all charge states.

Transverse Component of the Starting Energy given by Potential Φ_0

start potential for the different cases:

case	2	3	4	5	6	7	8	
Fig.	6	7	8	9	10	11	12	
Φ_0	0.5	100	125	75	50	25	10	[Volt]

number of trajectories in different sections:

case / section	1	2	3	4	5	6	7
2	15600	3507	3459	295	295	165	133
3	15600	3518	3459	2802	1574	169	160
4	15600	3817	2321	946	947	900	891
5	15600	3916	2154	898	898	738	609
6	15600	3642	2577	1226	1266	1177	1050
7	15600	3511	2827	1414	1414	1405	1349
8	15600	3522	3114	1769	1770	1596	1589

electrical current (mA) in each section:

section / case	2	3	4	5	6	7	8	experiment
1	137.0	153.0	159.0	150.0	147.1	144.1	143.1	156.0
2	94.2	96.6	90.0	102.7	106.4	116.7	128.7	
3	94.1	40.4	38.1	46.0	52.5	58.5	73.9	55.0
4	—	—	38.1	46.0	52.5	58.5	73.9	
5	33.5	38.5	30.8	40.7	50.4	58.2	66.4	
6	—	—	25.9	35.9	44.8	55.8	66.2	
7	17.6	31.2	16.7	25.6	33.4	46.5	51.5	
7*	11.9	21.2	11.4	17.4	22.7	31.6	35.0	25.0

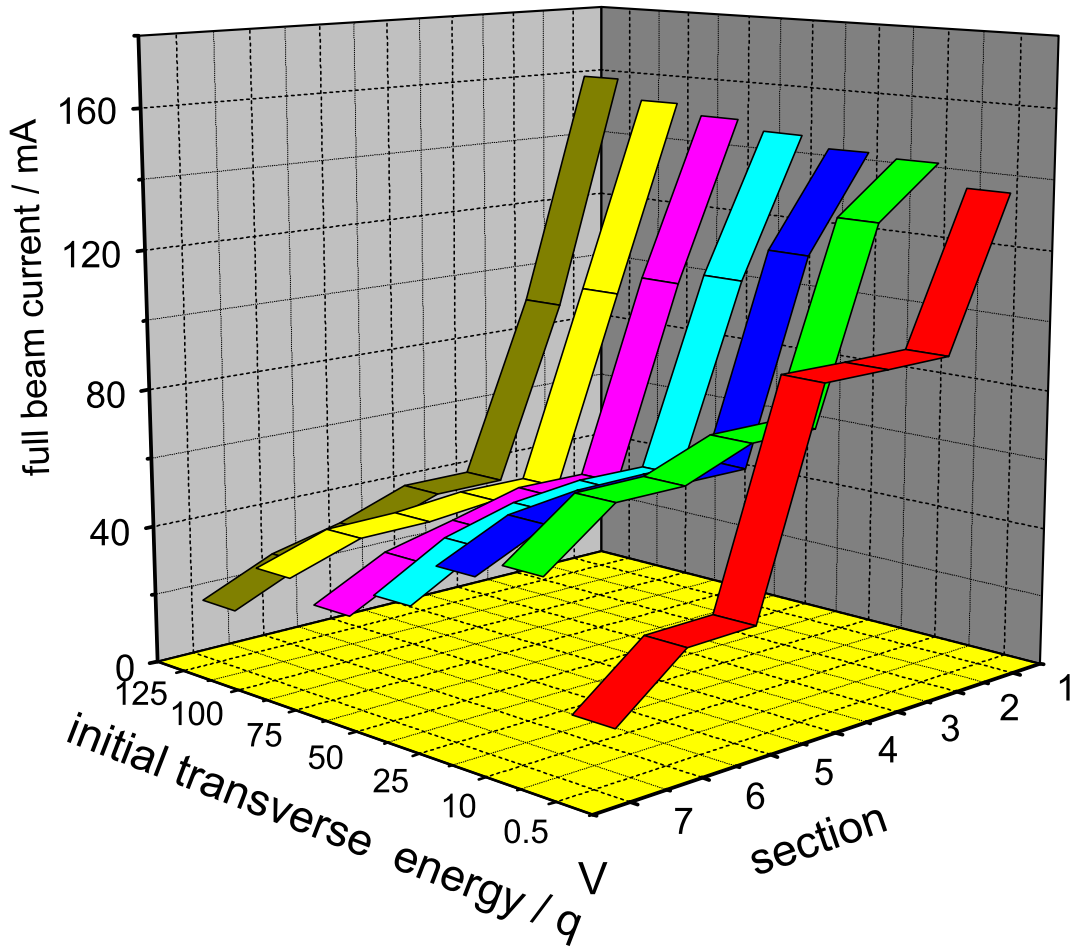Section 7^* is the charge state corrected current for $^{238}U^{4+}$.

Fig. 1: Current along the beam line for the cases with different transverse initial energy, using the potential model. The notation on axis represents the virtual potential drop in which all charge states gain there starting energy.

From Fig. 1 the following conclusions can be drawn:

- A slightly increasing extraction current with increasing initial transverse energy is obtained.

- According to the simulation first losses take place within the extraction tube. This fact could be used for diagnostic reasons.

- Strong losses appear when entering the acceleration gap. This is because no lens is used in this section between extraction and further acceleration. The beam emittance has a focal point within the extraction, and, with a plausible aperture diameter of the entrance electrode to the acceleration gap, the maximum tolerable angle is below 30 mrad. The current injected into the acceleration gap could be increased by reducing the distance ion source to acceleration gap or with a suitable lens on high potential.

- With higher initial transverse energy less current can be injected into the acceleration gap.

- If the current within the acceleration gap becomes unmatched, the angle becomes such as high that part of the beam will be lost in the quadrupole transport beam line. The matched condition is achieved when the beam current corresponds to the transverse electric field in the acceleration gap. Otherwise over-focusing for the case of low current will happen or the diameter becomes too large for the case that the current is too high. It should be pointed out, that the beam divergence increases for both cases: the under-dense case, as well as the over-dense case compared to the matched condition [12].

- Experimental tools like the moveable gap or the possibility to optimize the beam line setting by tuning the quadrupole gradients have not been used in the simulation.

- Because of the strong space charge force in the acceleration gap the beam has such a large diameter and divergence at the entrance of the quadrupole triplet that losses are unavoidable.

- Similar conditions are present in the following doublet in which the beam has to be transformed from a large diameter, low divergence state to a focal point in the horizontal plane and about parallel in the vertical plane.

- In most of the simulations losses occur in the de-focusing plane in all quadrupoles because of the large diameter of the beam.

- Comparing the experimental current values along the beam line with the simulation data case 6 and case 7 fit best with the experiment. Together with the measurement of the longitudinal component of the energy and this simulation we conclude that the angle of emission from the cathode should be in the range from $\arcsin\sqrt{25/160}\ldots\arcsin\sqrt{50/160}$, respectively $23^o\ldots34^o$.

Transverse Component of the Starting Energy given by Momentum

start velocity for the different cases:

case	9	10	11	12
Fig.	13	14	15	16
β	$3.8 \cdot 10^{-5}$	$3.8 \cdot 10^{-5}$	$3.0 \cdot 10^{-5}$	$2.6 \cdot 10^{-5}$

number of trajectories in different sections:

case / section	1	2	3	4	5	6	7
9	15600	3610	2631	1236	1236	1216	1167
10	15600	4018	2550	1154	1155	1082	980
11	15600	3913	2409	1076	1076	899	787
12	15600	3864	2466	1157	1157	1072	948

electrical current (mA) in each section:

section / case	9	10	11	12
1	146.0	165.0	158.3	156.3
2	110.0	104.6	97.9	98.7
3	54.5	48.3	43.4	46.3
4	54.5	48.3	43.4	46.3
5	53.5	45.4	36.0	42.7
6	51.6	41.3	31.2	37.8
7	44.0	29.8	20.8	28.3
7*	29.9	20.3	14.1	19.2

Section 7^* is the charge state corrected current for $^{238}U^{4+}$.

Further conclusions can be drawn:

- Case 9 for the momentum model is a not physical, because it is a mix between both models: whereas the longitudinal velocity component is distributed with the potential model, the transverse velocity component is defined by the momentum model.

- The difference between both models is not fundamental; in both cases the divergence of the beam is the main reason for losses. This is valid for the losses at the entrance aperture of the acceleration gap and for the losses within the quadrupole lenses behind the acceleration gap. However, the best suitable initial velocity components are different for both models. It should be pointed out again, that under experimental condition this initial angle cannot be influenced.

- A remarkable difference in beam transport because of the difference in the ratio of initial velocities has not been found.

- Comparing the experimental current values along the beam line with the simulation data case 12 fits best with the experiment. Together with the measurement of the longitudinal component of the energy and this simulation we conclude that the angle of emission from the cathode should be about $\arcsin(18.75/40) \approx 30^o$.
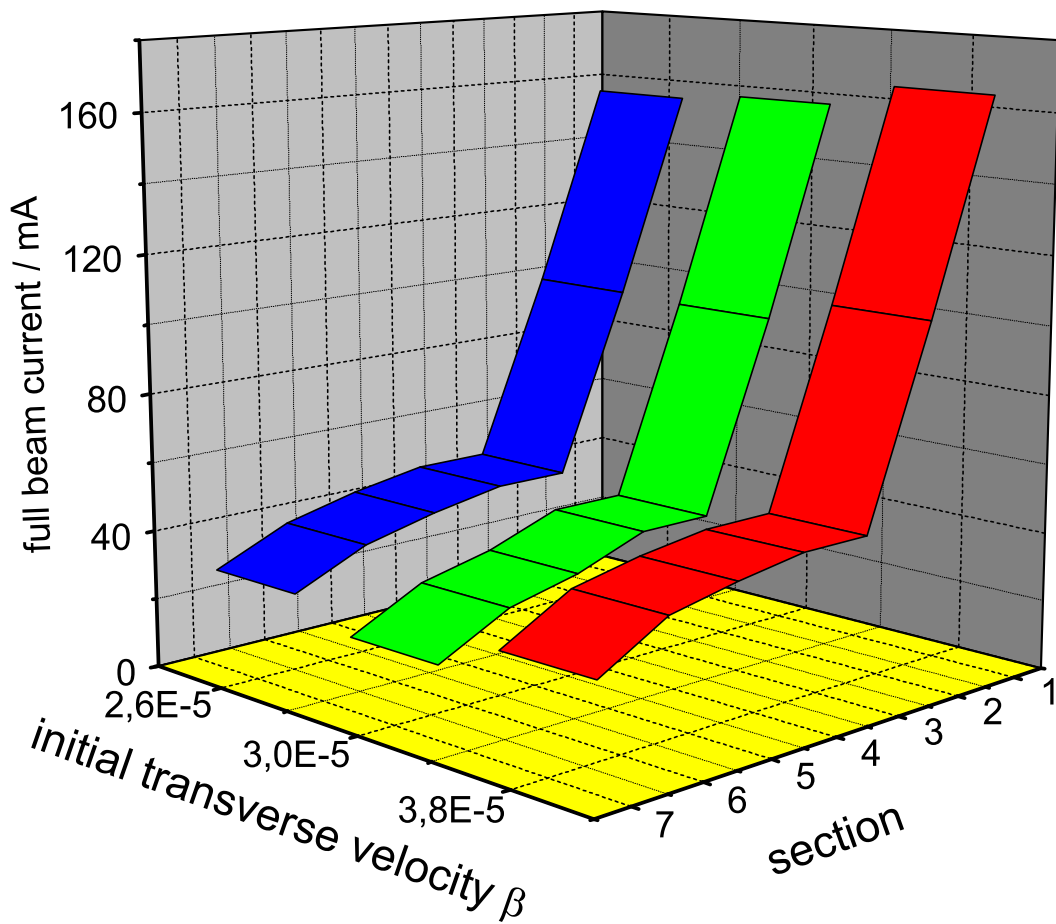
Fig. 2: Electrical current along the beam line for the momentum model. The notation on axis represents the initial starting velocity. Depending on the transverse component of the momentum the angle for each trajectory is modified.

Transmission

To improve the beam quality it is desirable to minimize transmission losses. In the following figure the phase space coordinates of the starting coordinates are displayed. Particles which are lost within this section are shown in dark color, whereas transmitted particles are shown in light color. Each figure shows the transmission within one section: extraction system, drift, and acceleration.

- Figure 3 shows that extraction is made from the undisturbed plasma.

- Figures 4 and 5 indicate that it should be possible to increase the current in the gap by increasing the number of extraction holes. This can be seen in the phase space plot, drawing a virtual acceptance ellipse around the transmitted trajectories. However, one should keep in mind that the total extracted current would be increased from 150 mA to 220 mA.

- Figures 6-16 are the individual cases, showing the full data in the horizontal plane (bottom) and in the vertical plane (top). Each figure shows from left to right the ion source, drift section, acceleration gap, drift section, five magnetic quadrupole lenses.

Fig. 3: Transmission of the extraction system

KOBRA3-INP

transmission plot

iteration 19

phase space y

phase space z

real space

angle space
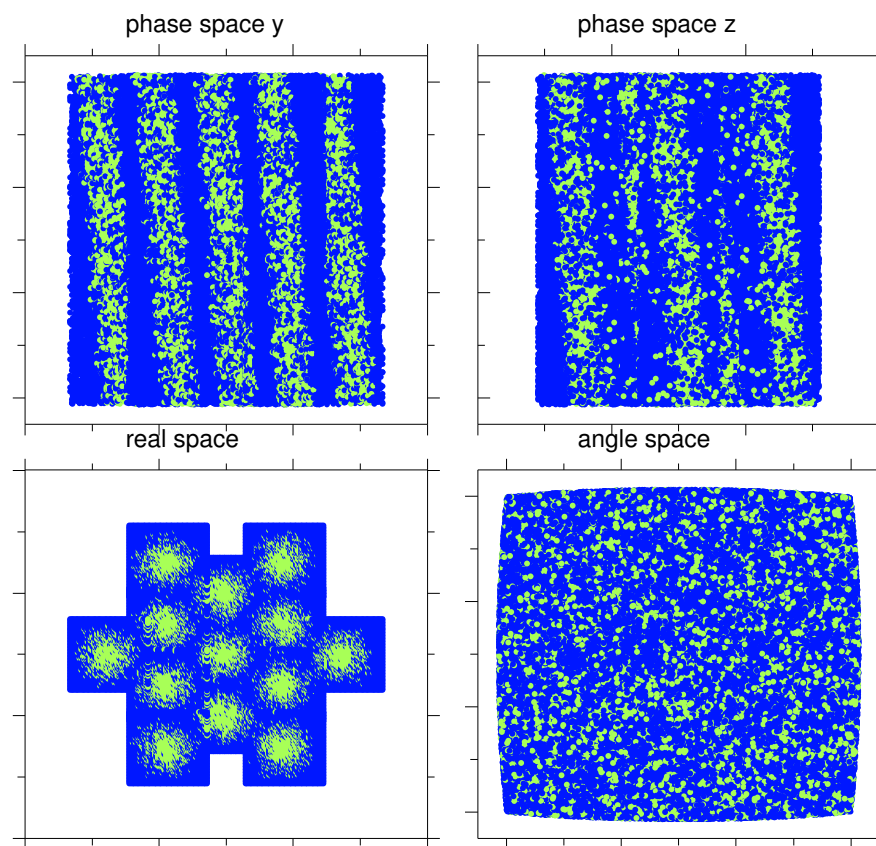
mevva extraction-01,700mA,160eV/q,100eV/
file: F:/inp/data/kobra/xiangwei/mevva/section 1 hr/PLOT002.EPS

date: 27/04/2004   time: 20:55:34
user: INP Wiesbaden

Fig. 4: Transmission of the drift towards the acceleration gap

KOBRA3-INP

transmission plot

iteration 1

phase space y

phase space z

real space

angle space
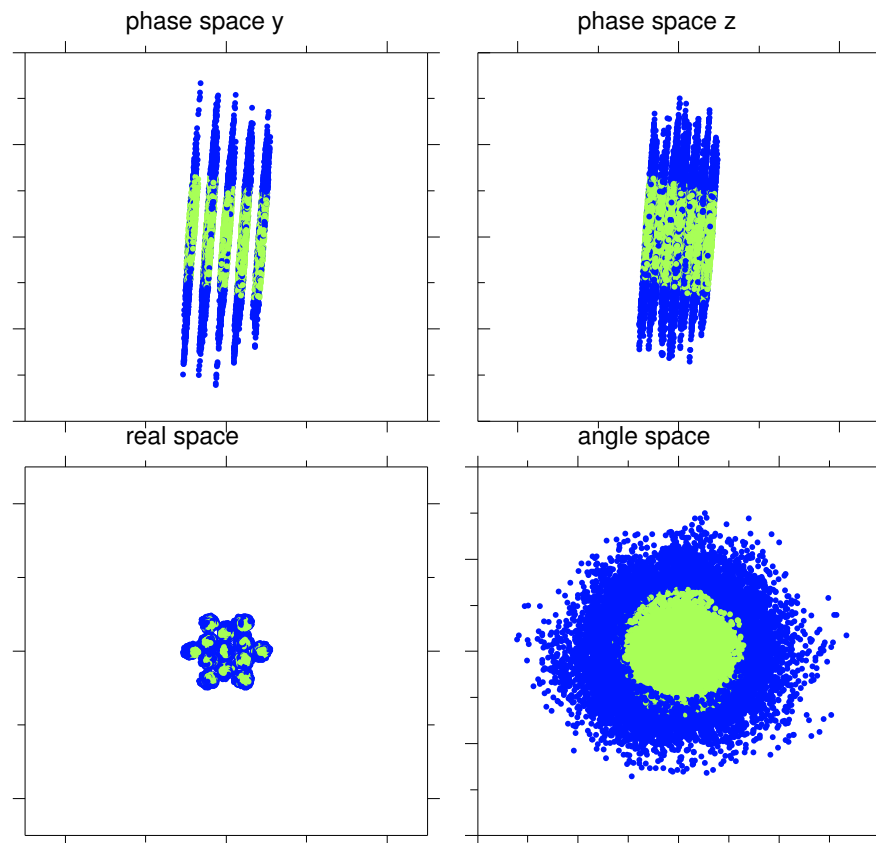
mevva section 2 mit extraktionsrohr
file: F:/inp/data/kobra/xiangwei/mevva/section 2/PLOT014.EPS

date: 27/04/2004   time: 21:27:29
user: INP Wiesbaden

KOBRA3-INP

transmission plot

iteration 47

phase space y

phase space z

real space

angle space
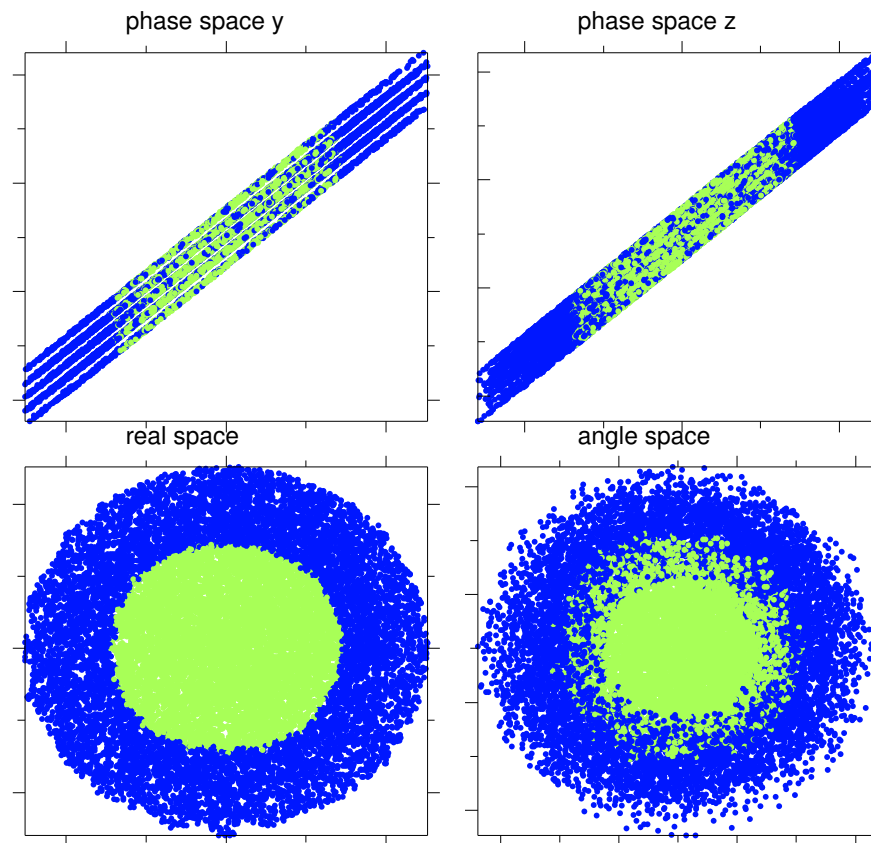
mevva section 3-700mA,160eV,0.5eV
file: F:/inp/data/kobra/xiangwei/mevva/section 3/PLOT127.EPS

date: 27/04/2004   time: 21:44:37
user: INP Wiesbaden

Fig. 6: potential model

X
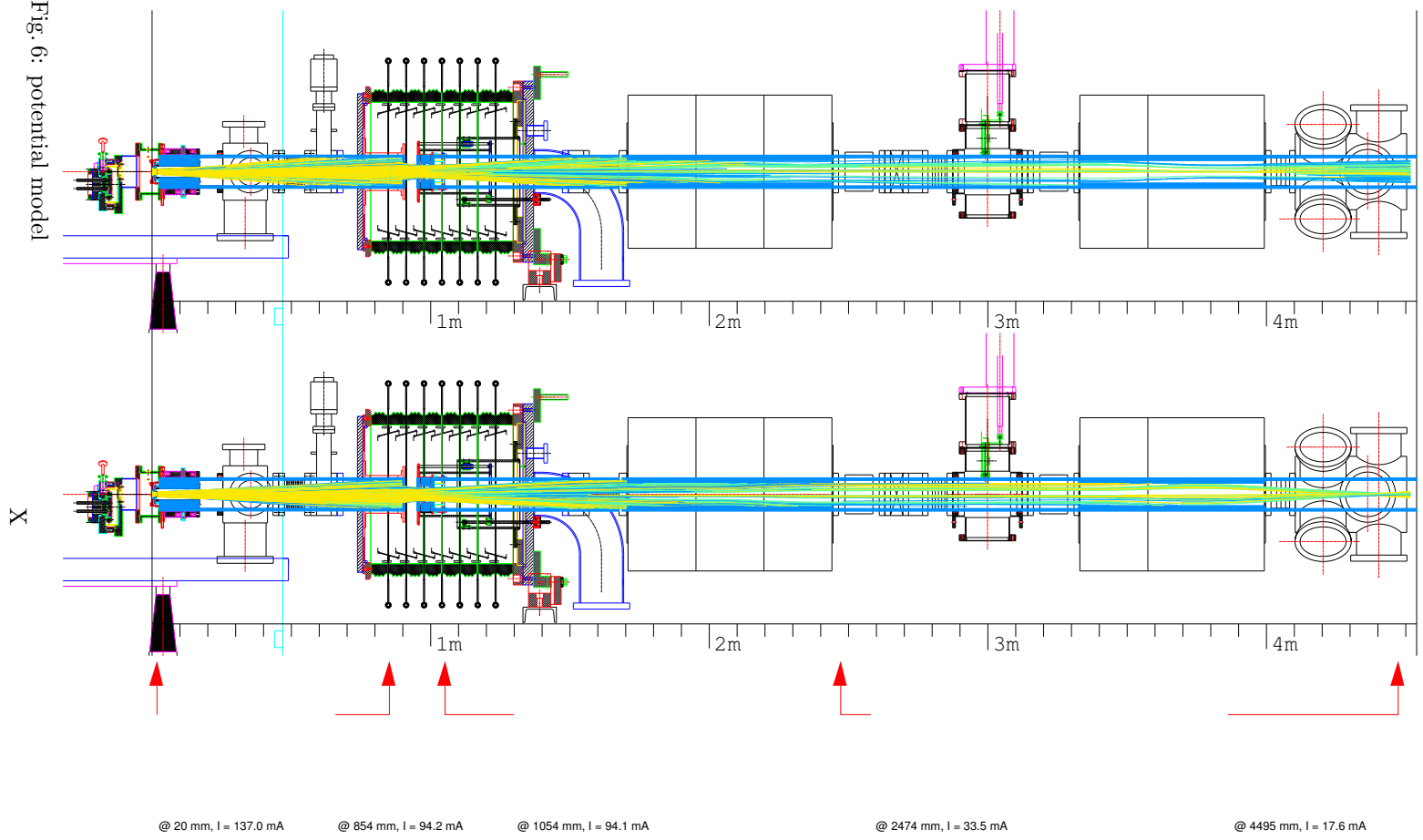
MEVVA parameter case002

start energy from potential

	simulation	
mesh	201 x 151 x 151 dist: 0.1/0.2/0.2mm	
	168 x 61 x 61	5/2/2mm
	201 x 61 x 61	1/2/2mm
	121 x 61 x 61	5/2/2mm
	201 x 61 x 61	4/2/2mm
	206 x 61 x 61	4/2/2mm
	312 x 61 x 61	4/2/2mm
trajectories	15600	
plasma potential	50V	
ion energy (long./trans.)	160V*q/0.5V*q	
	extraction	
geometry	13 x 3mm	
potentials	32/-2/0kV	
current per hole [33.64 mm²]	U³⁺	0.00945 A
	U⁴⁺	0.0329 A
	U⁵⁺	0.00614 A
	post acceleration	
screening voltage	-3.9 kV	
high voltage	100.010 kV	
	beam transport	
QT [gradient × length]	-0.6149 T, 1.3534 T, -0.8914 T	
QD [gradient × length]	1.0018 T, -1.6639 T	

@ 20 mm, I = 137.0 mA   @ 854 mm, I = 94.2 mA   @ 1054 mm, I = 94.1 mA   @ 2474 mm, I = 33.5 mA   @ 4495 mm, I = 17.6 mA

Fig. 7: potential model

XI

MEVVA parameter case003

start energy from potential

	simulation		
mesh	201 x 151 x 151 dist: 0.1/0.2/0.2mm		
	168 x 61 x 61	5/2/2mm	
	201 x 61 x 61	1/2/2mm	
	121 x 61 x 61	5/2/2mm	
	201 x 61 x 61	4/2/2mm	
	206 x 61 x 61	4/2/2mm	
	312 x 61 x 61	4/2/2mm	
trajectories	15600		
plasma potential	50V		
ion energy (long./trans.)	160V*q/100V*q		
	extraction		
geometry	13 x 3mm		
potentials	32/-2/0kV		
current per hole [33.64 mm²]	U³⁺	0.00945 A	
	U⁴⁺	0.0329 A	
	U⁵⁺	0.00614 A	
	post acceleration		
screening voltage	-3.9 kV		
high voltage	100.010 kV		
	beam transport		
QT [gradient × length]	-0.6149 T, 1.3534 T, -0.8914 T		
QD [gradient × length]	1.0018 T, -1.6639 T		

@ 20 mm, I = 153.0 mA   @ 854 mm, I = 96.6 mA   @ 1054 mm, I = 40.4 mA   @ 1674 mm, I = mA   @ 2474 mm, I = 38.5 mA   @ 4495 mm, I = 31.2 mA

Fig. 8: potential model

XII

MEVVA parameter case004

start energy from potential

	simulation	
mesh	201 x 151 x 151 dist: 0.1/0.2/0.2mm	
	168 x 61 x 61	5/2/2mm
	201 x 61 x 61	1/2/2mm
	121 x 61 x 61	5/2/2mm
	201 x 61 x 61	4/2/2mm
	206 x 61 x 61	4/2/2mm
	312 x 61 x 61	4/2/2mm
trajectories		15600
plasma potential		50V
ion energy (long./trans.)		160V*q/125V*q
	extraction	
geometry		13 x 3mm
potentials		32/-2/0kV
current per hole [33.64 mm²]	U³⁺	0.00945 A
	U⁴⁺	0.0329 A
	U⁵⁺	0.00614 A
	post acceleration	
screening voltage		-3.9 kV
high voltage		100.010 kV
	beam transport	
QT [gradient × length]		-0.6149 T, 1.3534 T, -0.8914 T
QD [gradient × length]		1.0018 T, -1.6639 T

@ 20 mm, I = 159.0 mA   @ 854 mm, I = 90.0 mA   @ 1054 mm, I = 38.1 mA   @ 1674 mm, I = 38.1 mA   @ 2474 mm, I = 30.8 mA   @ 3294 mm, I = 25.9 mA   @ 4495 mm, I = 16.7 mA

MEVVA parameter case005

start energy from potential

	simulation		
mesh	201 x 151 x 151 dist: 0.1/0.2/0.2mm		
	168 x 61 x 61	5/2/2mm	
	201 x 61 x 61	1/2/2mm	
	121 x 61 x 61	5/2/2mm	
	201 x 61 x 61	4/2/2mm	
	206 x 61 x 61	4/2/2mm	
	312 x 61 x 61	4/2/2mm	
trajectories	15600		
plasma potential	50V		
ion energy (long./trans.)	160V*q/75V*q		
	extraction		
geometry	13 x 3mm		
potentials	32/-2/0kV		
current per hole [33.64 mm²]	U^{3+}	0.00945 A	
	U^{4+}	0.0329 A	
	U^{5+}	0.00614 A	
	post acceleration		
screening voltage	-3.9 kV		
high voltage	100.010 kV		
	beam transport		
QT [gradient × length]	-0.6149 T, 1.3534 T, -0.8914 T		
QD [gradient × length]	1.0018 T, -1.6639 T		

@ 20 mm, I = 150.0 mA   @ 854 mm, I = 102.7 mA   @ 1054 mm, I = 46.0 mA   @ 1674 mm, I = 46.0 mA   @ 2474 mm, I = 40.7 mA   @ 3294 mm, I = 35.9 mA   @ 4495 mm, I = 25.6 mA

Fig. 10: potential model

MEVVA parameter case006

start energy from potential

	simulation	
mesh	201 x 151 x 151 dist: 0.1/0.2/0.2mm	
	168 x 61 x 61	5/2/2mm
	201 x 61 x 61	1/2/2mm
	121 x 61 x 61	5/2/2mm
	201 x 61 x 61	4/2/2mm
	206 x 61 x 61	4/2/2mm
	312 x 61 x 61	4/2/2mm
trajectories		15600
plasma potential		50V
ion energy (long./trans.)		160V*q/50V*q
	extraction	
geometry		13 x 3mm
potentials		32/-2/0kV
current per hole [33.64 mm²]	U³⁺	0.00945 A
	U⁴⁺	0.0329 A
	U⁵⁺	0.00614 A
	post acceleration	
screening voltage		-3.9 kV
high voltage		100.010 kV
	beam transport	
QT [gradient × length]		-0.6149 T, 1.3534 T, -0.8914 T
QD [gradient × length]		1.0018 T, -1.6639 T

@ 20 mm, I = 147.1 mA   @ 854 mm, I = 106.4 mA   @ 1054 mm, I = 52.5 mA   @ 1674 mm, I = 52.5 mA   @ 2474 mm, I = 50.4 mA   @ 3294 mm, I = 44.8 mA   @ 4495 mm, I = 33.4 mA

Fig. 11: potential model

XV
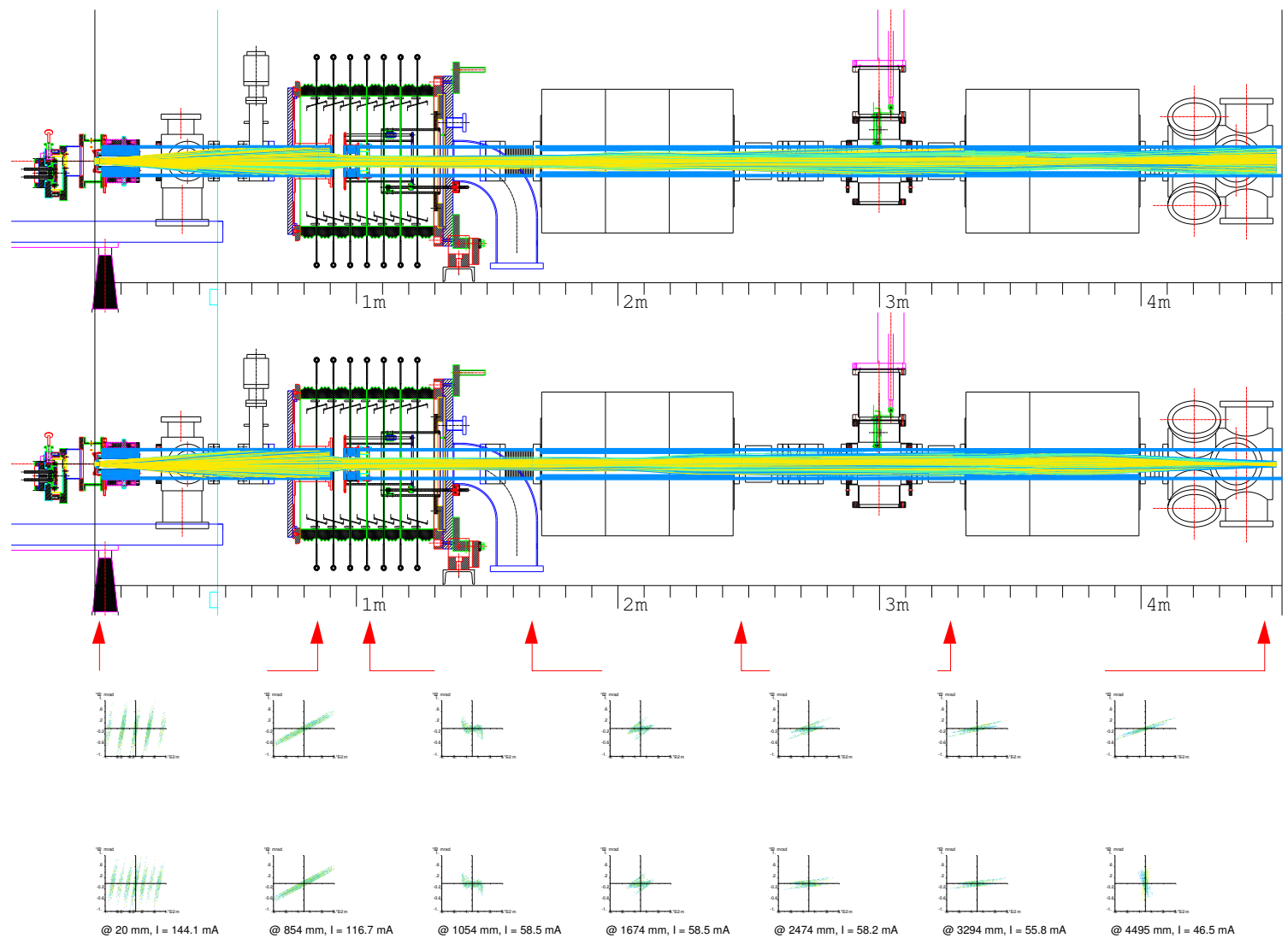
MEVVA parameter case007

start energy from potential

		simulation
mesh		201 x 151 x 151 dist: 0.1/0.2/0.2mm
		168 x 61 x 61 5/2/2mm
		201 x 61 x 61 1/2/2mm
		121 x 61 x 61 5/2/2mm
		201 x 61 x 61 4/2/2mm
		206 x 61 x 61 4/2/2mm
		312 x 61 x 61 4/2/2mm
trajectories		15600
plasma potential		50V
ion energy (long./trans.)		160V*q/25V*q
		extraction
geometry		13 x 3mm
potentials		32/-2/0kV
current per hole [33.64 mm²]	U³⁺	0.00945 A
	U⁴⁺	0.0329 A
	U⁵⁺	0.00614 A
		post acceleration
screening voltage		-3.9 kV
high voltage		100.010 kV
		beam transport
QT [gradient × length]		-0.6149 T, 1.3534 T, -0.8914 T
QD [gradient × length]		1.0018 T, -1.6639 T

@ 20 mm, I = 144.1 mA   @ 854 mm, I = 116.7 mA   @ 1054 mm, I = 58.5 mA   @ 1674 mm, I = 58.5 mA   @ 2474 mm, I = 58.2 mA   @ 3294 mm, I = 55.8 mA   @ 4495 mm, I = 46.5 mA

Fig. 12: potential model

XVI

MEVVA parameter case008

start energy from potential

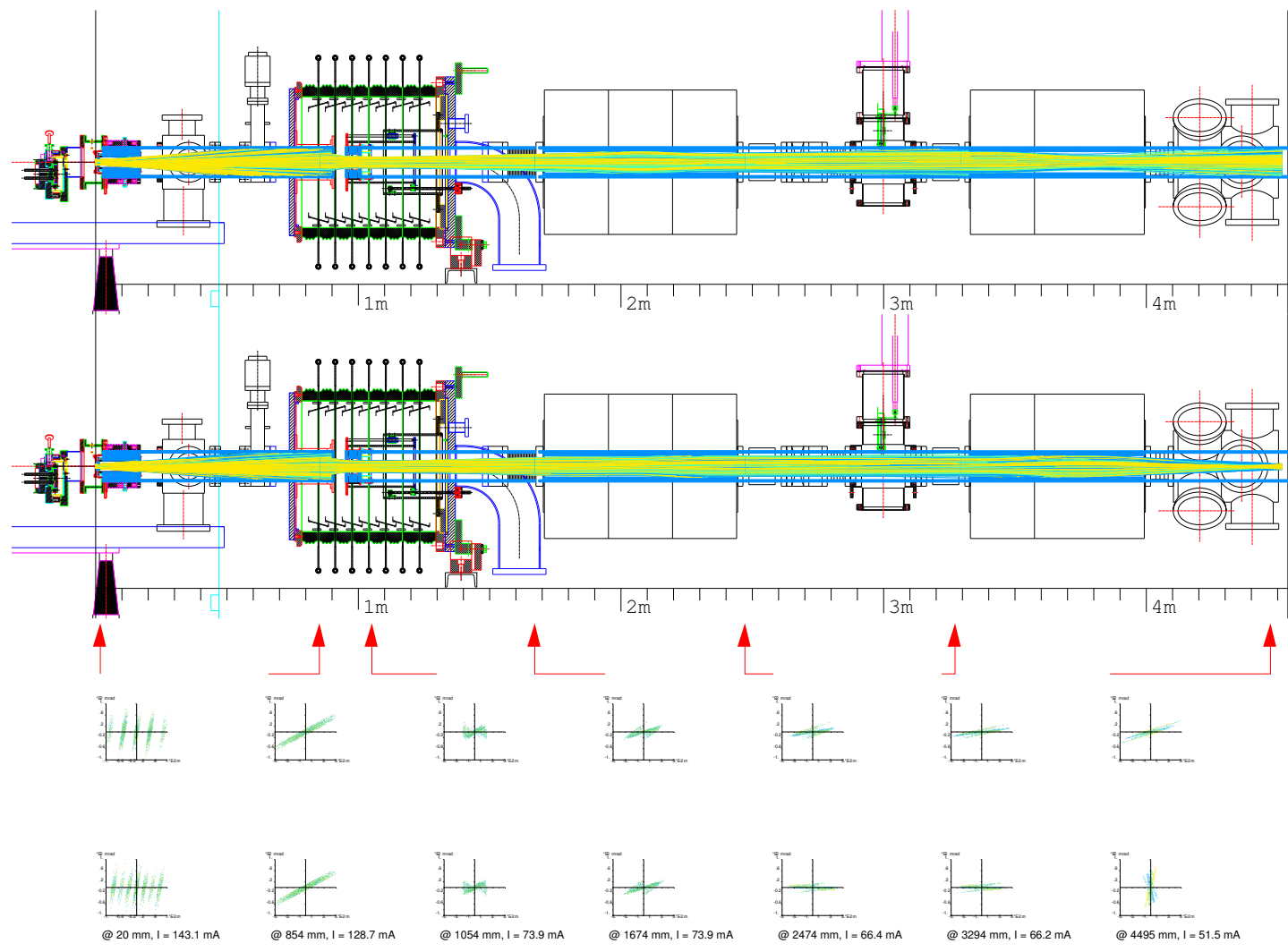| simulation	
mesh	201 x 151 x 151 dist: 0.1/0.2/0.2mm
	168 x 61 x 61 5/2/2mm
	201 x 61 x 61 1/2/2mm
	121 x 61 x 61 5/2/2mm
	201 x 61 x 61 4/2/2mm
	206 x 61 x 61 4/2/2mm
	312 x 61 x 61 4/2/2mm
trajectories	15600
plasma potential	50V
ion energy (long./trans.)	160V*q/10V*q
extraction	
geometry	13 x 3mm
potentials	32/-2/0kV
current per hole [33.64 mm²] U³⁺	0.00945 A
U⁴⁺	0.0329 A
U⁵⁺	0.00614 A
post acceleration	
screening voltage	-3.9 kV
high voltage	100.010 kV
beam transport	
QT [gradient × length]	-0.6149 T, 1.3534 T, -0.8914 T
QD [gradient × length]	1.0018 T, -1.6639 T

@ 20 mm, I = 143.1 mA   @ 854 mm, I = 128.7 mA   @ 1054 mm, I = 73.9 mA   @ 1674 mm, I = 73.9 mA   @ 2474 mm, I = 66.4 mA   @ 3294 mm, I = 66.2 mA   @ 4495 mm, I = 51.5 mA

Fig. 13: mixing of potential model with momentum model XVII
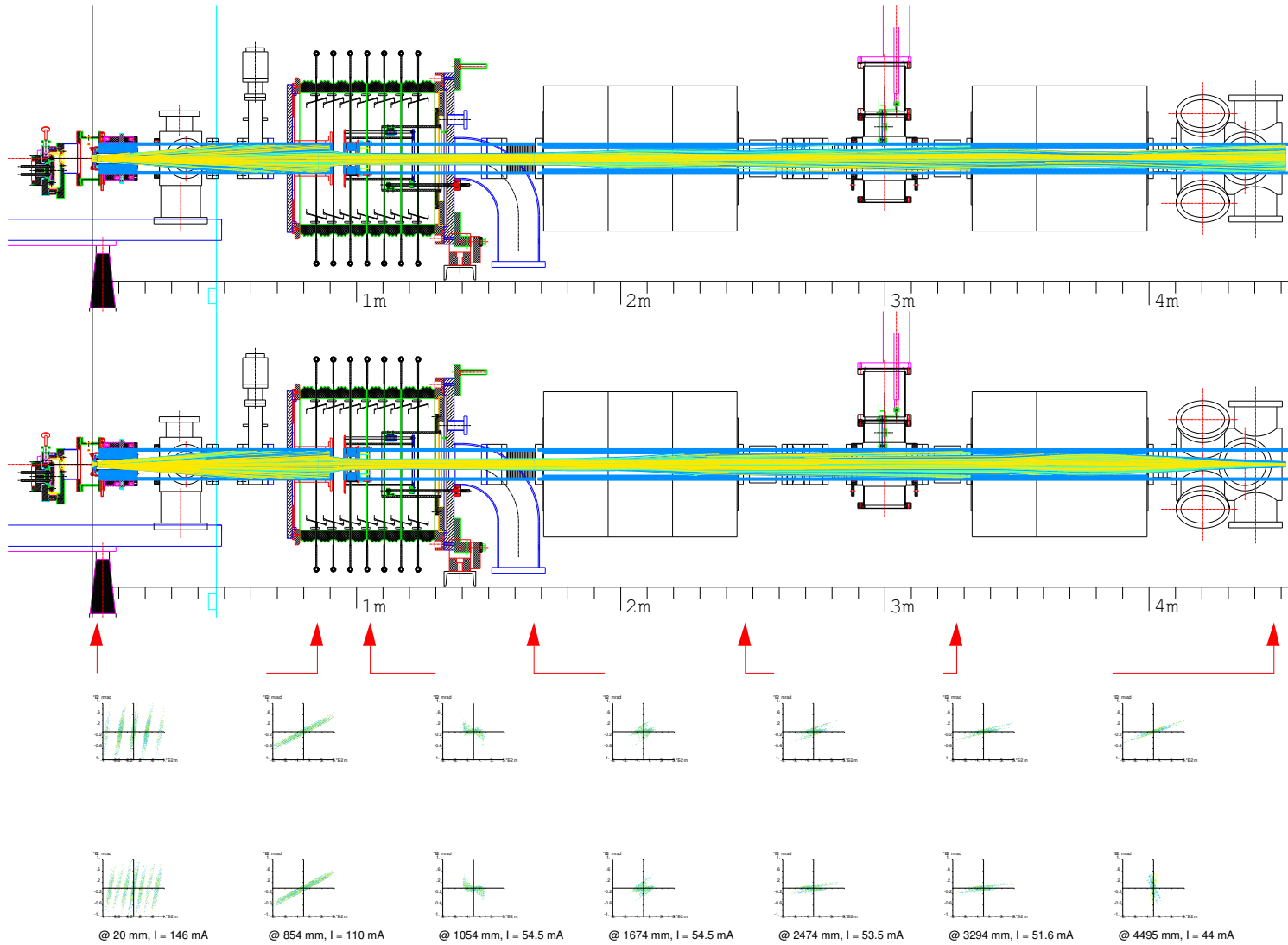
MEVVA parameter case009

start energy from momentum

simulation		
mesh	201 x 151 x 151	0.1/0.2/0.2mm
	168 x 61 x 61	5/2/2mm
	201 x 61 x 61	1/2/2mm
	121 x 61 x 61	5/2/2mm
	201 x 61 x 61	4/2/2mm
	206 x 61 x 61	4/2/2mm
	312 x 61 x 61	4/2/2mm
trajectories		15600
plasma potential		50V
ion energy (long./trans.)	160/53.33eV–40eV-32eV	
extraction		
geometry		13 x 3mm
potentials		32/-2/0kV
current per hole [33.64 mm²]	U³⁺	0.00945 A
	U⁴⁺	0.0329 A
	U⁵⁺	0.00614 A
post acceleration		
screening voltage		-3.9 kV
high voltage		100.010 kV
beam transport		
QT [gradient × length]	-0.6149 T, 1.3534 T, -0.8914 T	
QD [gradient × length]	1.0018 T, -1.6639 T	

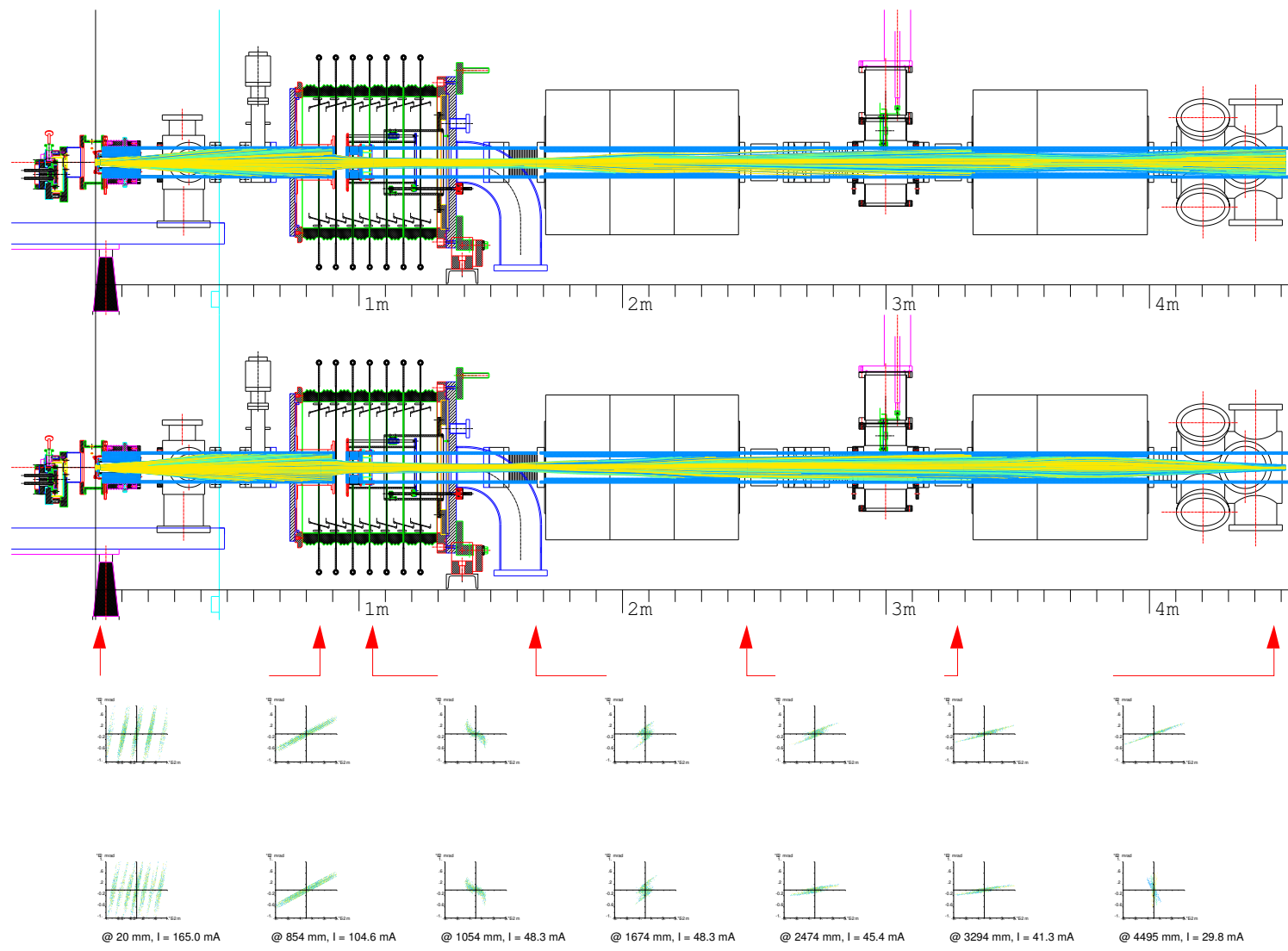@ 20 mm, I = 146 mA   @ 854 mm, I = 110 mA   @ 1054 mm, I = 54.5 mA   @ 1674 mm, I = 54.5 mA   @ 2474 mm, I = 53.5 mA   @ 3294 mm, I = 51.6 mA   @ 4495 mm, I = 44 mA

XVIII

MEVVA parameter case010

start energy from momentum

simulation		
mesh	201 x 151 x 151 dist: 0.1/0.2/0.2mm	
	168 x 61 x 61	5/2/2mm
	201 x 61 x 61	1/2/2mm
	121 x 61 x 61	5/2/2mm
	201 x 61 x 61	4/2/2mm
	206 x 61 x 61	4/2/2mm
	312 x 61 x 61	4/2/2mm
trajectories		15600
plasma potential		50V
ion energy (long./trans.)	53.33-40-32eV/53.33eV-40eV-32eV	
extraction		
geometry		13 x 3mm
potentials		32/-2/0kV
current per hole [33.64 mm²]	U^{3+}	0.00945 A
	U^{4+}	0.0329 A
	U^{5+}	0.00614 A
post acceleration		
screening voltage		-3.9kV
high voltage		100.010 kV
beam transport		
QT [gradient × length]	-0.6149 T, 1.3534 T, -0.8914 T	
QD [gradient × length]	1.0018 T, -1.6639 T	

@ 20 mm, I = 165.0 mA   @ 854 mm, I = 104.6 mA   @ 1054 mm, I = 48.3 mA   @ 1674 mm, I = 48.3 mA   @ 2474 mm, I = 45.4 mA   @ 3294 mm, I = 41.3 mA   @ 4495 mm, I = 29.8 mA
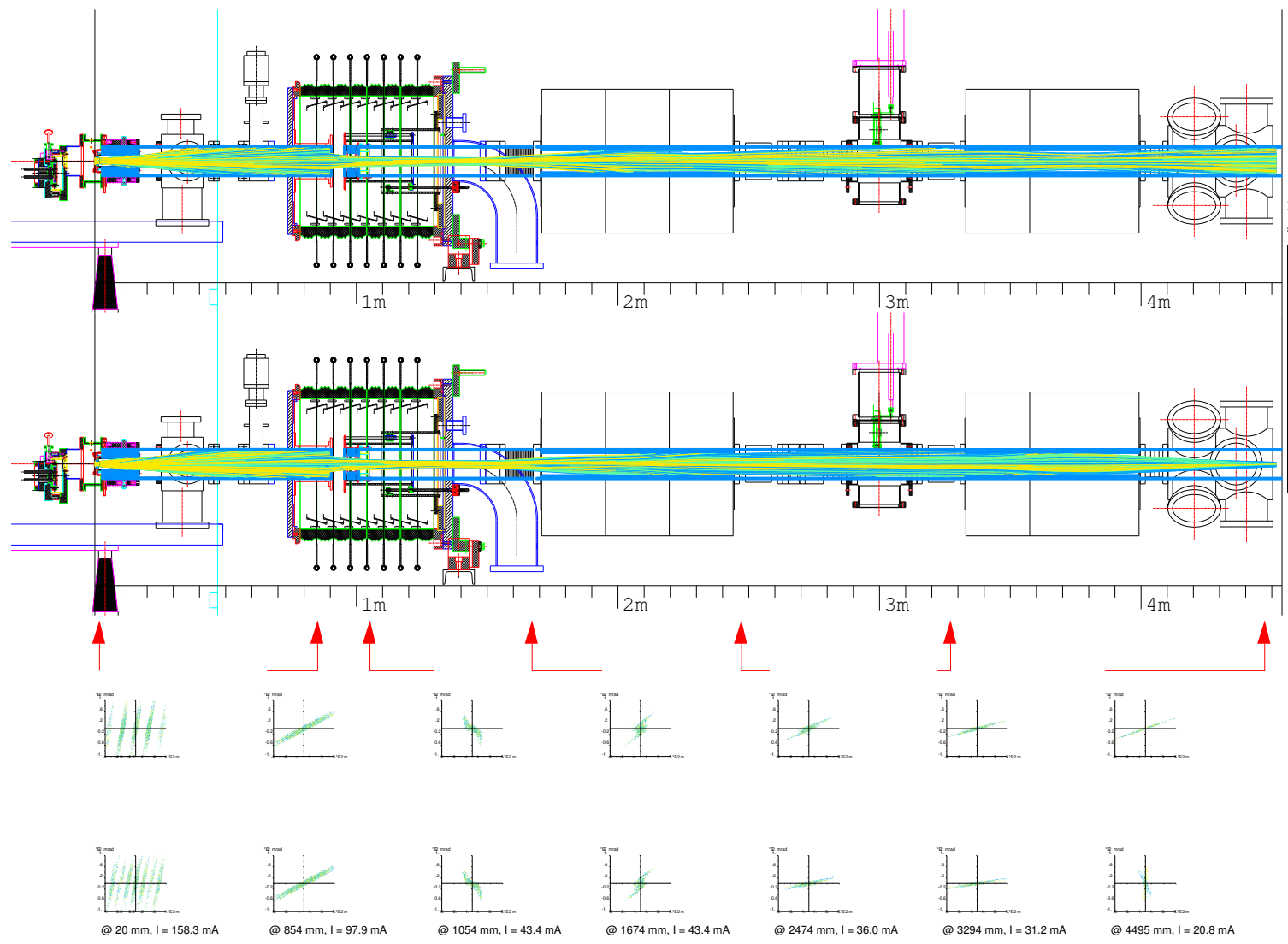
Fig. 15: momentum model

XIX

MEVVA parameter case011

start energy from momentum

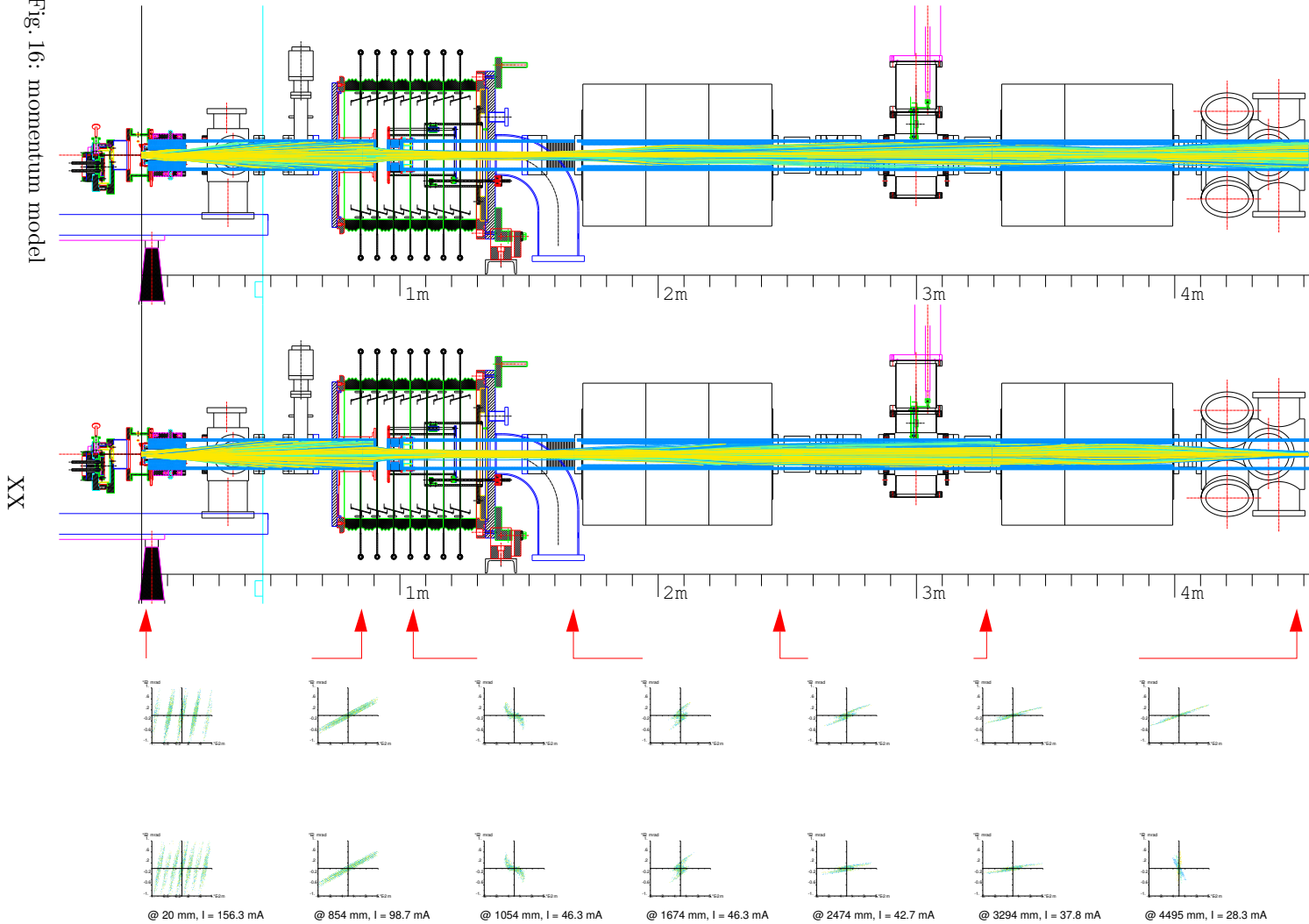|	simulation	
mesh	201 x 151 x 151 dist: 0.1/0.2/0.2mm	
	168 x 61 x 61	5/2/2mm
	201 x 61 x 61	1/2/2mm
	121 x 61 x 61	5/2/2mm
	201 x 61 x 61	4/2/2mm
	206 x 61 x 61	4/2/2mm
	312 x 61 x 61	4/2/2mm
trajectories		15600
plasma potential		50V
ion energy (long./trans.)	43.33-40-32eV/32eV-25eV-20eV	
	extraction	
geometry		13 x 3mm
potentials		32/-2/0kV
current per hole [33.64 mm²]	U³⁺	0.00945 A
	U⁴⁺	0.0329 A
	U⁵⁺	0.00614 A
	post acceleration	
screening voltage		-3.9kV
high voltage		100.010kV
	beam transport	
QT [gradient × length]	-0.6149 T, 1.3534 T, -0.8914 T	
QD [gradient × length]	1.0018 T, -1.6639 T	

@ 20 mm, I = 158.3 mA   @ 854 mm, I = 97.9 mA   @ 1054 mm, I = 43.4 mA   @ 1674 mm, I = 43.4 mA   @ 2474 mm, I = 36.0 mA   @ 3294 mm, I = 31.2 mA   @ 4495 mm, I = 20.8 mA

Fig. 16: momentum model

XX

MEVVA parameter case012

start energy from momentum

simulation		
mesh	201 x 151 x 151 dist: 0.1/0.2/0.2mm	
	168 x 61 x 61	5/2/2mm
	201 x 61 x 61	1/2/2mm
	121 x 61 x 61	5/2/2mm
	201 x 61 x 61	4/2/2mm
	206 x 61 x 61	4/2/2mm
	312 x 61 x 61	4/2/2mm
trajectories		15600
plasma potential		50V
ion energy (long./trans.)	43.33-40-32eV/25eV-18.75eV-15eV	
extraction		
geometry		13 x 3mm
potentials		32/-2/0kV
current per hole [33.64 mm²]	U^{3+}	0.00945 A
	U^{4+}	0.0329 A
	U^{5+}	0.00614 A
post acceleration		
screening voltage		-3.9 kV
high voltage		100.010 kV
beam transport		
QT [gradient × length]	-0.6149 T, 1.3534 T, -0.8914 T	
QD [gradient × length]	1.0018 T, -1.6639 T	

@ 20 mm, I = 156.3 mA   @ 854 mm, I = 98.7 mA   @ 1054 mm, I = 46.3 mA   @ 1674 mm, I = 46.3 mA   @ 2474 mm, I = 42.7 mA   @ 3294 mm, I = 37.8 mA   @ 4495 mm, I = 28.3 mA